Marine Geology 439 (2021) 106565

Contents lists available at ScienceDirect

Marine Geology

journal homepage: www.elsevier.com/locate/margo

Late Quaternary high-resolution seismic stratigraphy and core-based paleoenvironmental reconstructions in Ona Basin, southwestern Scotia Sea (Antarctica)

Adrián López-Quirós [a,b,*], Francisco J. Lobo [b], Meghan Duffy [c], Amy Leventer [c], Dimitris Evangelinos [b], Carlota Escutia [b], Fernando Bohoyo [d]

[a] Department of Geoscience, Aarhus University, Høegh-Guldbergs Gade 2, 8000 Aarhus C, Denmark
[b] Instituto Andaluz de Ciencias de la Tierra, CSIC-UGR, Avda. de las Palmeras 4, Armilla, 18100 Granada, Spain
[c] Department of Geology, Colgate University, Hamilton, NY, USA
[d] Instituto Geológico y Minero de España, Ríos Rosas, 23, 28003 Madrid, Spain

ARTICLE INFO

Editor: Michele Rebesco

Keywords:
Late Quaternary
LGM
Deglaciation
Seismic stratigraphy
Diatom assemblage
Scotia Sea
Antarctica

ABSTRACT

The variability of sedimentation patterns and processes driven by late Quaternary glacial-interglacial paleoclimatic and paleoceanographic changes are investigated in Ona Basin, southwestern Scotia Sea. The interest of this area lies in the fact that the nearby Antarctic Peninsula has recorded extreme climatic variability, and the Drake Passage-Scotia Sea oceanic domain is influenced by two major Southern Ocean water masses, the eastward-flowing Antarctic Circumpolar Current (ACC) and the westward-flowing Weddell Sea Deep Water (WSDW). These goals are achieved through the examination of a grid of very high-resolution sub-bottom profiles and two gravity cores collected in Ona Basin. Multi-proxy data derived from the gravity cores include ^{14}C-derived ages, descriptions of sedimentary units and diatom assemblages, and continuous logging of physical properties and micro-XRF core scanning.

The sub-surface seismic stratigraphy is composed of four seismic units (U4 to U1) with a dominant sub-parallel configuration, with local occurrence of wavy facies and intercalations of transparent seismic facies. Additionally, four sedimentary units were recognized through sediment core analysis from bottom to top: Unit IV is composed of slightly bioturbated diatom-rich mud and silty mud with sparse ice-rafted debris (IRDs); Unit III is composed of gravelly silty to sandy mud with large amounts of IRDs; Unit II mostly contains bioturbated diatomaceous mud; and Unit I is composed of diatom-rich silty to sandy mud. The highest diatom abundances are found in Unit II, whereas highly variable abundances are found in Unit IV. The most common diatoms are *Fragilariopsis kerguelensis* and *Chaetoceros* subg. *Hyalochaete*. Overall, these characteristics document a change in the depositional style from terrigenous during the Last Glacial Maximum (LGM) to hemipelagic sedimentation during the deglaciation.

The high-resolution seismic stratigraphy analysis reveals significant fluctuations in the regional bottom-current patterns during the late Quaternary (i.e., after 0.4 Ma) glacial-interglacial cycles. An overall strengthening of the westward-flowing WSDW is postulated in relation to latitudinal displacements of the interphase between the deeper ACC and the WSDW, together with enhanced interactions between along- and downslope processes. In addition, sedimentological, geochemical, and micropaleontological analyses revealed two distinctive phases during the late Pleistocene, in terms of paleoenvironments and paleoceanographic conditions. During the LGM, extensive sea-ice coverage limited biogenic productivity in the ocean. Increased terrigenous input was largely supplied by the westward-flowing WSDW, under a reduced ACC influence due to the northward location of fronts. During deglaciation, the sediment record indicates reduced sea-ice cover and increased open-ocean conditions and surface water productivity, as well as a long-term intensification of the WSDW flow. We postulate bottom-current strengthening was driven by an increased Weddell Sea water export and the southward migration of fronts as a consequence of major retreat of sea ice, enhancing the ACC influence in the southern Ona Basin, and thus, affecting the sloping interphase between the deeper ACC and the WSDW.

* Corresponding author at: Department of Geoscience, Aarhus University, Høegh-Guldbergs Gade 2, 8000 Aarhus C, Denmark.
E-mail address: alquiros@geo.au.dk (A. López-Quirós).

https://doi.org/10.1016/j.margeo.2021.106565
Received 26 February 2021; Received in revised form 10 June 2021; Accepted 9 July 2021
Available online 17 July 2021

1. Introduction

Interactions between the Southern Ocean and the Antarctic ice sheet have been profoundly controlled by glacial-interglacial climate variability during the late Quaternary (Bae et al., 2003; Kim et al., 2020). The Drake Passage-Scotia Sea has long been considered a key area to better understand and constrain these interactions, since diverse studies have revealed the influence of changing climatic conditions in nearby continental shelf areas, such as the northern Antarctic Peninsula (e.g., Anderson et al., 2002; Leventer et al., 2002; Lucchi et al., 2002; Pudsey, 2000; Shevenell and Kennett, 2002; Gersonde et al., 2003; Vaughan et al., 2003; Ó Cofaigh et al., 2005; Heroy and Anderson, 2005; Evans et al., 2005; Bentley et al., 2009), which together with Patagonia have acted as main regional sediment source areas (Diekmann et al., 2000; Wu et al., 2019). The periodic waxing and waning of marine-based ice sheets in the Scotia Sea, located along the iceberg escape route from the Weddell Sea (Anderson and Andrew, 1999; Diekmann and Kuhn, 1999) (Fig. 1), could have provided a plausible sediment transport mechanism through iceberg-rafted debris (IRDs) (Shin et al., 2020). Once in the marine environment, sediment transport patterns are interpreted to have been mostly driven by the eastward-flowing Antarctic Circumpolar Current (ACC) and Weddell Sea Deep Water (WSDW) derived from the Weddell Gyre or their ancient counterparts. This fact is evidenced by the occurrence of extensive sediment drifts in several Scotia Sea basins (e.g.,

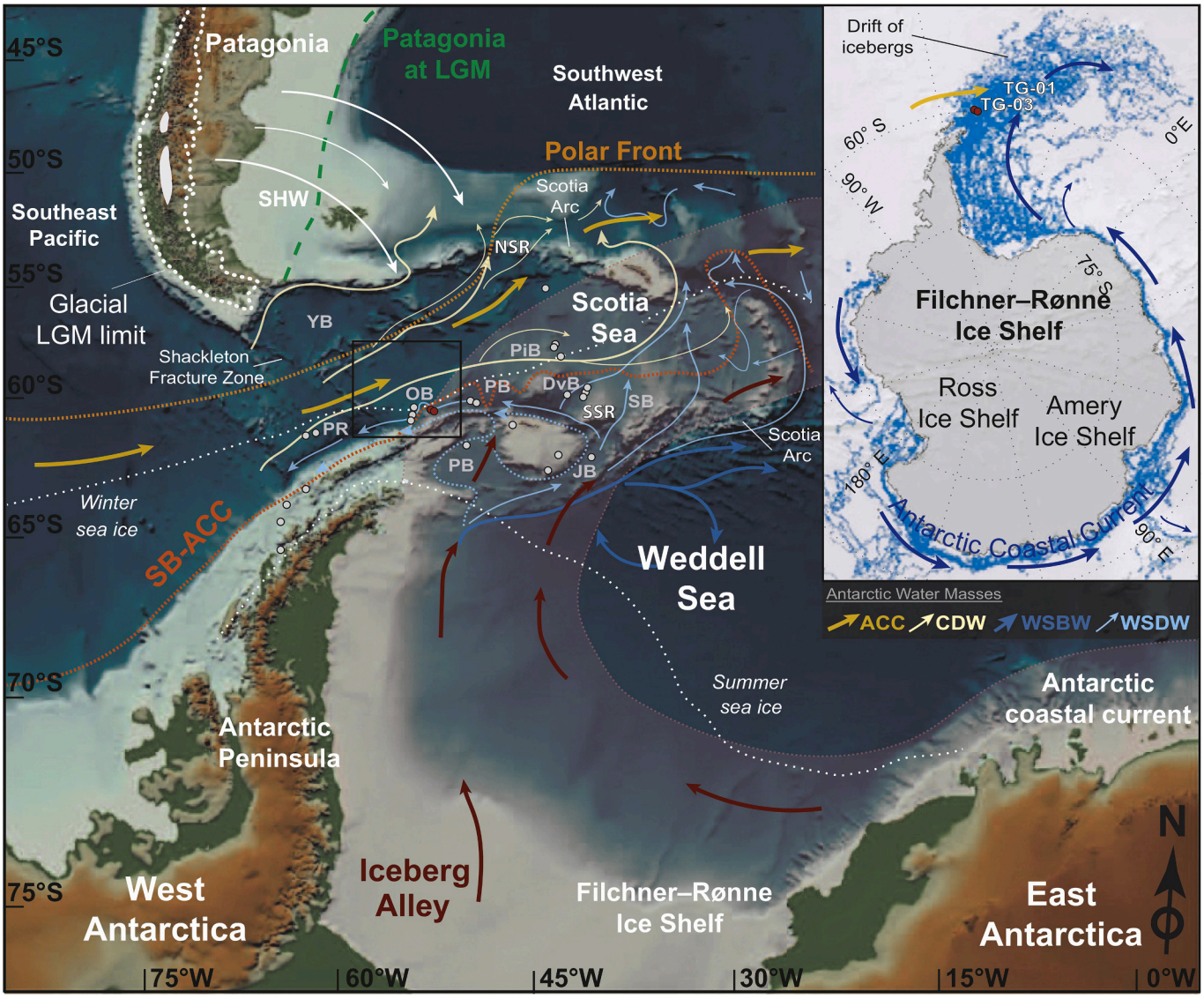

Fig. 1. Overview of ocean circulation in the Drake Passage region, showing the small basins in the southern Scotia Sea and the location of Ona Basin (squared area) in the southwestern Scotia Sea. Modified after Weber et al. (2014) with permission from Springer. PR: Phoenix region; YB: Yaghan Basin; OB: Ona Basin; PB: Protector Basin; PiB: Pirie Basin; DvB: Dove Basin; SB: Scan Basin; PB: Powell Basin; JB: Jane Basin. The location of sediment cores examined in the present study (cores TG-01 and TG-03; red dots) and cores analyzed in previous studies (gray dots) are indicated. See Figure 3B for complete information of available sediment cores in the study region. The red arrows within the reddish shadow region indicate the location of Iceberg Alley from Anderson and Andrew (1999). The Southern Hemisphere westerlies (SHW) are indicated by white arrows. The white dotted line marks the limit of Patagonian ice sheet during the Last Glacial Maximum (LGM) (Hein et al., 2010), while the green dashed line indicates the maximum extent of Patagonia at the LGM (Iriondo, 2000). The light orange dotted line indicates the Polar Front (PF), while the dark orange dotted line is the Southern Boundary of the Antarctic Circumpolar Current (SB-ACC) (e.g., Orsi et al., 1995; Diekmann et al., 2000). White dotted lines indicate winter and summer sea ice extent (Gersonde et al., 2005). The map in the upper-right corner shows the circum-Antarctic drift of icebergs calving off the Antarctic ice shelves from 1999 to 2009 (Stuart and Long, 2011). ACC: Antarctic Circumpolar Current; CDW: Circumpolar Deep Water; WSBW: Weddell Sea Bottom Water; WSDW: Weddell Sea Deep Water; NSR: North Scotia Ridge; SSR: South Scotia Ridge. (For interpretation of the references to colour in this figure legend, the reader is referred to the web version of this article.)

Maldonado et al., 2003, 2006, 2014; Martos et al., 2013; García et al., 2016; Pérez et al., 2014, 2017, 2019; López-Quirós et al., 2020), which increased in significance since the late Miocene (Pérez et al., 2021) and which have continued to develop up to the present-day (Pudsey and Howe, 2002).

Most of these studies are based on multichannel seismic data, which comprise long temporal scales and do not provide sufficient resolution to resolve short-term fluctuations of these water masses during the late Quaternary. However, the changing conditions have been recorded in a periodic alternation of depositional processes; thus, increased detrital materials have been deposited preferentially during glacial conditions, whereas hemipelagic sediments with an abundant biogenic fraction have accumulated during interglacials, in connection with strengthening of contour current flows (Presti et al., 2011; Jimenez-Espejo et al., 2020; Holder et al., 2020).

In the Drake Passage-Scotia Sea region, limited sediment core data also reveal that glacial-interglacial variability has modulated the prevailing pattern of terrigenous sediment transport from emerged areas (e.g., Diekmann et al., 2000; Weber et al., 2012), and the influence of glacigenic processes and ocean circulation on biological productivity and marine sedimentation processes (e.g., Yoon et al., 2009; Lee et al., 2012; Xiao et al., 2016). Specifically, the most recent transition from the Last Glacial Maximum (LGM) to the Holocene has been accompanied by significant oceanographic changes involving variations of the intensity and spatial extent of ACC and WSDW flows (Pudsey and Howe, 2002; Kim et al., 2020). This transition, triggered by changes in insolation and ice melting (Clark et al., 2012; Golledge et al., 2014; DeConto and Pollard, 2016), is a key time interval that provides contrasting boundary conditions for future projections in global climate (see IPCC, 2019).

Ona Basin, the westernmost of the southern Scotia Sea basins, is an ideal location to assess paleoenvironmental changes in response to ice dynamics and paleoceanographic changes driven by glacial/interglacial alternations. This basin is located close to the northern tip of the Antarctic Peninsula, a region sensitive to climate variations, and thus can provide important insights into the ice-ocean interactions during the late Quaternary. In addition, Ona Basin is affected by both ACC and WSDW flows (e.g., Naveira Garabato et al., 2002a; Morozov et al., 2010) (Fig. 1), which have fluctuated from the LGM to the Holocene in response to ice-sheet (Kim et al., 2020) and oceanic front dynamics (Wu et al., 2019). Specifically, the WSDW, the densest variety of the Antarctic Bottom Water, extends to the southern Scotia Sea (Fig. 1); this cold and dense bottom water supplies terrigenous material to the region (Maldonado et al., 2003).

The main objective of this study is to characterize the late Quaternary paleoceanographic conditions prevailing in the southwestern Scotia Sea, based on high-resolution seismic data and gravity cores collected in Ona Basin. Our findings are also compared with results from the western Drake Passage-Scotia Sea region in order to provide a comprehensive view of the glacial-interglacial changes in the Drake Passage-Scotia Sea region during the late Quaternary.

2. Study area

2.1. Geological and stratigraphic setting

The Scotia Sea, located between South America and the Antarctic Peninsula, comprises at present the Scotia and Sandwich plates, which are limited by the Shackleton Fracture Zone (SFZ) to the west and by the tectonic Scotia Arc boundaries on the three remaining sides (Fig. 1). The South Scotia Ridge (SSR) constitutes the plate boundary between the Scotia and Antarctic plates. Present-day tectonic activity along the SSR is characterized by major transcurrent structures with transpressional regime in the western part and transtensional regime in the central and eastern parts (Pelayo and Wiens, 1989; Galindo-Zaldivar et al., 1996; Bohoyo et al., 2007; Bohoyo et al., 2019). The southern Scotia Sea, north of the SSR, contains a series of small oceanic basins developed during the Scotia Arc formation since the Late Eocene, from west to east: Ona, Protector, Pirie, Dove, and Scan basins (see review by Pérez et al., 2019, and references therein) (Fig. 1).

Ona Basin, north of the SSR and Elephant Island shelf and south of the West Scotia Ridge (WSR) extinct spreading center, is the westernmost intra-oceanic basin of the southern Scotia Sea (Figs. 1 and 2A). This basin is bounded by the SFZ to the west and Terror Bank to the east, while to the north it opens into the western Scotia Sea abyssal plain and is separated from the southern Yaghan Basin by the WSR (Fig. 2A). Ona Basin is subdivided in two sub-basins, western and eastern, by a submarine structural high designated as the 'Ona High' (Maldonado et al., 2014) (Fig. 2).

The Ona Basin acoustic basement is marked by a high-amplitude seismic horizon tilted to the southwest and fragmented by NNW-SSE to WNW-ESE structures, interpreted as normal, reverse and transcurrent faults (e.g., Civile et al., 2012; Maldonado et al., 2014) (Fig. 2). The stratigraphic architecture of Ona Basin includes eight main seismic units (VIII to I from bottom to top) above the acoustic basement (Martos et al., 2013; Maldonado et al., 2014; Pérez et al., 2019) (Fig. 2B). *Reflector-c* is a regional unconformity (recently dated as >8.4 Ma; Pérez et al., 2021; Fig. 2B) that represents a major shift in the Scotia Sea stratigraphy related to the inflow of Antarctic Bottom Water from the Weddell Sea and the northward expansion of the West Antarctic and Antarctic Peninsula ice sheets (Anderson et al., 2011). In Ona Basin, *reflector-c* divides the stratigraphic record into older and younger units (Fig. 2B). The older units (VIII to IV) are deformed and controlled mainly by basement structures, while the youngest units (III to I) display only local deformation (Maldonado et al., 2014; Pérez et al., 2019). These younger units contain abundant evidences of sediment drift development under the combined influence of the ACC and the WSDW (e.g., Maldonado et al., 2006; Martos et al., 2013; Maldonado et al., 2014; Pérez et al., 2014, 2019; García et al., 2016; López-Quirós et al., 2020). Unit I above *reflector-a* displays a sheet-like geometry and its tentative chronology was recently updated as Early Pleistocene (~1.7 Ma) to Recent (Pérez et al., 2021) (Fig. 2B). Furthermore, a minor internal discontinuity referred to as *reflector-a'* distinguishes a local, uppermost subunit over the Ona High (Pérez et al., 2019; Fig. 2B), recently dated as Middle Pleistocene (~0.4 Ma) to Recent (Pérez et al., 2021) (Fig. 2B).

2.2. Oceanographic setting

The Scotia Sea is influenced by water masses derived from the Drake Passage and the Weddell Sea, via the eastward-flowing ACC and the northern limb of the Weddell Gyre, respectively (Fig. 1). The boundaries of different ACC jets are constituted by four deep-reaching hydrographic fronts (Orsi et al., 1995) that are strongly conditioned by the Scotia Sea topography (Tarakanov, 2012): (1) the Sub-Antarctic front (SAF), (2) the Polar front (PF), (3) the Southern ACC front (SACCF) and the Southern Boundary of the ACC (SB-ACC) (e.g. Fig. 1). The Circumpolar Deep Water (CDW) propagates from west to east in the field of the ACC (Naveira Garabato et al., 2002a; Tarakanov, 2010).

The Weddell Sea Deep Water (WSDW) is a subset of the Antarctic Bottom Water (AABW) (Orsi et al., 1999; Naveira Garabato et al., 2002a) and one of the deepest water masses flowing in the cyclonic Weddell Gyre above the Weddell Sea Bottom Water (WSBW) (e.g., Naveira Garabato et al., 2002a; Gordon et al., 2010). In the Weddell Gyre, many icebergs merge and eventually escape from Antarctica north into the Scotia Sea through the so-called 'Iceberg Alley' (Anderson and Andrew, 1999) (Fig. 1). A fraction of the WSDW circulates from the Weddell Sea to the Scotia Sea mainly through Jane Basin, flowing across several deep gateways of the SSR into the Scotia Sea, as the Orkney Passage (Orsi et al., 1999; Naveira Garabato et al., 2002a, 2002b; Palmer et al., 2012) (Fig. 1). A branch of the WSDW flows westwards along the northern slopes of the SSR, as the northern South Orkney Microcontinent, and reaches the Pacific-West Antarctica margin (Naveira Garabato et al., 2002a, 2002b; Heywood et al., 2004; Legg et al., 2009) (Fig. 1).

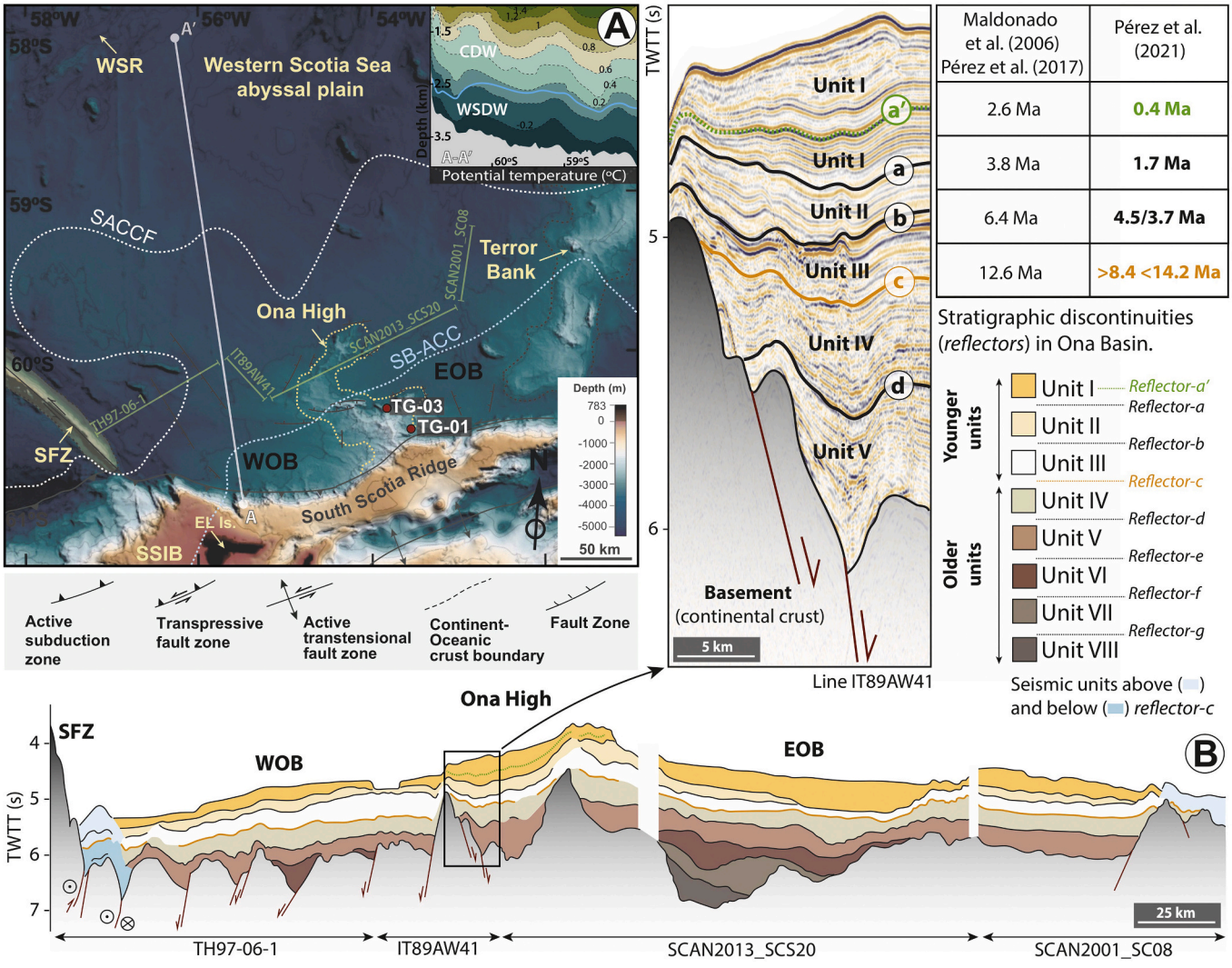

Geophysical cruise	*RV OGS-Explora* (1990) Italy	*RV Hakurei-Maru* (1997) Japan	*BIO Herpérides* (2001) Spain	*BIO Herpérides* (2013) Spain
Seismic lines	IT89AW41	TH97-06-1	SCAN2001_SC08	SCAN2013_SCS20
Energy source	Airguns (volume 45.18L)	GI-guns (volume 65.55L)	Airguns BOLT (volume 29.6L)	Airguns BOLT (volume 8.5L)
Marine streamer	Length 2975m, 120 channels	Length 3000m, 240 channels	Length 2400m, 96 channels	Length 250m, 3 channels

Fig. 2. Geomorphological and seismic stratigraphic characterization of Ona Basin. A) Ona Basin is subdivided into eastern and western Ona sub-basins (EOB and WOB, respectively) by the Ona High. The panel in the upper-right corner displays the A-A' profile, in which the vertical distribution of potential temperature (°C) and distribution of major water masses (CDW and WSDW) with depth are shown (modified from Morozov et al., 2010). Locations of studied cores TG-01 and TG-03 (red dots) are indicated. Bathymetry is extracted from the DBM-BATDRAKE compilation (Bohoyo et al., 2019). Tectonic features in the map extracted from Maldonado et al. (2014), after Civile et al. (2012). SSIB: South Shetland Island Block; EL. Is: Elephant Island; WSR: West Scotia Ridge; SFZ: Shackleton Fracture Zone; SACCF: Southern ACC front; SB-ACC: Southern Boundary of the ACC. B) Seismic stratigraphic profile across Ona Basin (extracted from Pérez et al., 2019). Profile location is indicated in Fig. 2A. The enlarged squared area corresponds to a multichannel seismic line segment showing the younger seismic units and stratigraphic discontinuities in Ona Basin. Ages of the main regional discontinuities since *reflector-c* in Ma are from Maldonado et al. (2006) and Pérez et al. (2017), recently updated by Pérez et al. (2021). (For interpretation of the references to colour in this figure legend, the reader is referred to the web version of this article.)

In Ona Basin, the upper part of the water column is occupied by the CDW (Fig. 2A), and flows eastwards into the northern region of the basin (Naveira Garabato et al., 2002a; Morozov et al., 2010) (Fig. 1). The different fronts of the ACC mark the southward extension of the CDW, and are characterized by strong eddy generation (Morozov et al., 2010) leading to an efficient mixing of the whole water mass (Provost et al., 2011). These eddies are originated from PF and SACCF meanders northwest of the physiographic highs that protrude from slopes in the southern region of the basin, such as Ona High and Terror Bank (Barré et al., 2011; Provost et al., 2011) (Fig. 2A). Below, the WSDW flows westwards along the southern part of the basin (Naveira Garabato et al., 2002a; Morozov et al., 2010) (Figs. 1 and 2A). The upward slope of the water masses towards the south (e.g., Sudre et al., 2011), determine that the southern Ona Basin is mostly affected by the westward-flowing WSDW (Fig. 2A). This flow is affected by northward deflections due to topographic obstacles (Morozov et al., 2010), and in the western Ona sub-basin it is constrained by the SFZ (e.g., Sudre et al., 2011) (Fig. 1).

2.3. *Recent sedimentary processes*

The southern margin of Ona Basin mainly contains a suite of contourite deposits that exhibit different configurations in response to the

westward propagation of the WSDW, which is able to generate different contourite erosional (i.e., contourite channels and moats) and depositional features (i.e., plastered, sheeted, mounded, fault-controlled, deformed and channel-related drifts, and superimposed sediment waves). The lateral continuity of these contourite features is interrupted by mass transport deposits and other gravity-driven features in and from Ona High. On the abyssal plain, extensive sheeted drifts with superimposed morphologies, such as sediment waves and mounded drifts were reported (López-Quirós et al., 2020). All these deep-water deposits have been recognized in the uppermost seismic unit above *reflector-a'*, and therefore they have been formed during the late Quaternary after 0.4 Ma (Pérez et al., 2021).

3. Materials and methods

This study is based on high-resolution seismic data and multi-proxy analysis of two sediment cores (TG-01 and TG-03; Fig. 3A). The data combination has great potential to provide key information for paleoenvironmental reconstructions and for detecting the influence of regional climate change. For such purposes, a compilation of previous investigated sediment coring sites in the southern Drake Passage-Scotia Sea region was also made to place our observations into a wider regional context (Fig. 3B). The high-resolution seismic dataset was collected on board the BIO Hespérides during expeditions SCAN 2004, 2008 and 2013 and DRAKE 2018 (Fig. 3A). During SCAN 2013, two gravity cores were collected in the Ona High slope, central Ona Basin, NE prolongation of the Antarctic Peninsula (Fig. 3A). Core TG-01 is 400 cm long and was collected at 2160 m water depth at 60°22′23.9314"S, 53°02′15.2501"W; core TG-03 is 295 cm long and was obtained at 2789 m water depth at 60°11′23.4003"S, 53°10′49.0810"W. Cores TG-01 and TG-03 were opened and split into two halves (working and archive), that were subsequently stored at 4 °C at the Geological Survey of Spain (IGME, Spain) core repository. Non-destructive analyses (i.e., visual core description, physical properties measurements and X-ray fluorescence scanning) were performed on the archive halves. Working halves were sampled for radiocarbon dating, sedimentological and micropaleontological analyses.

3.1. High-resolution seismic data

High-resolution seismic data were acquired with a Topographic Parametric Sonar (TOPAS) PS 18 system, which operated in a chirp wavelet (high-penetration mode) at primary frequencies of 1.5–5 kHz and a pulse length of 30 ms, providing a maximum vertical resolution of 0.2 ms. The collected signal was post-processed following standard processing with the TOPAS™ software (see details in López-Quirós et al., 2020). The resulting seismic data were converted and imported as SEG-Y files into IHS Kingdom Suite™ software for interpretation. About 6680 km of sub-bottom transects available for this study (Fig. 3A) provided a detailed high-resolution seismic stratigraphy of Ona Basin, where the TOPAS system could penetrate up to 150 m, assuming a seismic velocity of 1600 m/s for these shallow-water sediments (e.g., Schlesinger et al., 2012, and references therein). Seismic units defined in this study have been named from top to bottom, in order to provide a consistent naming pattern for the uppermost stratigraphic units that can be reproduced in other studies and to facilitate comparisons of stratigraphic patterns. The same labeling approach has been adopted by other seismic stratigraphic studies of different resolutions conducted in the Scotia Sea (e.g., Maldonado et al., 2006, 2014; Martos et al., 2013; Pérez et al., 2014, 2017, 2019). In addition, the recently revised seismic stratigraphy of the Scotia Sea by IODP Expedition 382 also has adhered to the top to bottom naming convention (Weber et al., 2021). Sedimentary units thickness descriptions are provided in milliseconds of TWTT (two-way travel time). Isochore maps of seismic units identified in this work were constructed only for the most recent units, since these units were detected in a higher number of seismic profiles.

3.2. Core chronology

Due to the absence of calcareous microfossils suitable for age dating in the studied sediment cores, three bulk sediment samples (20 cc in volume each, at 0.10, 2.30 and 2.60 m depths) from core TG-01 and two (20 cc in volume each, at 0.15 and 2.10 m depths) from core TG-03 were selected for Accelerator Mass Spectrometry (AMS) ^{14}C radiocarbon dating of acid-insoluble organic matter (AIOM). The selected samples were extracted from undisturbed intervals, avoiding sediment layers with evidences of sediment remobilization by gravity flows. Radiocarbon analysis was conducted in the Poznan Radiocarbon Laboratory

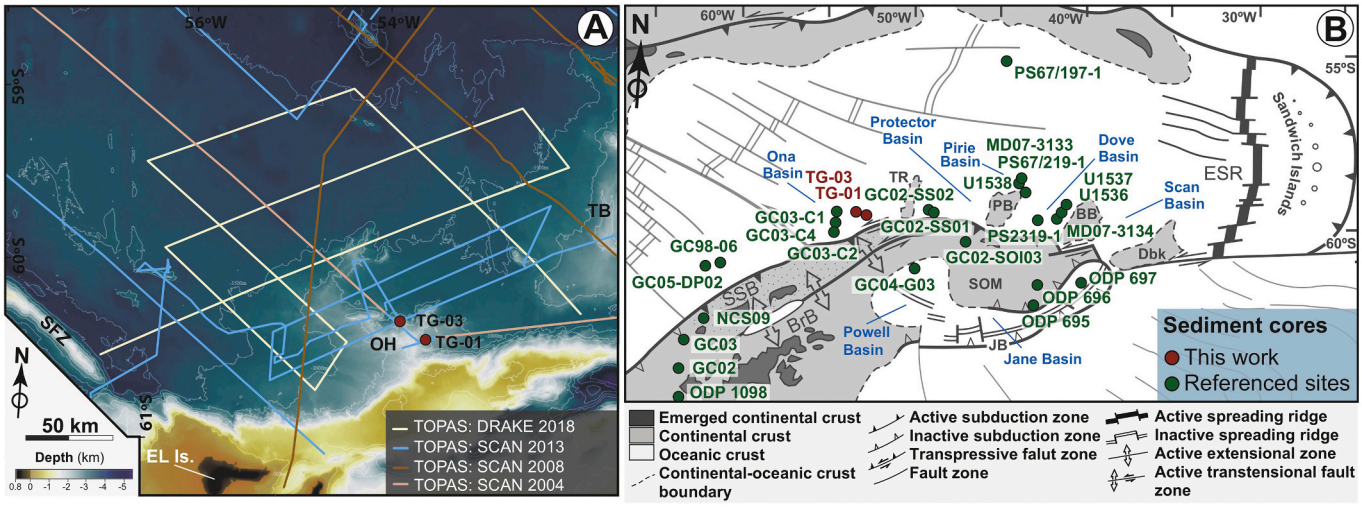

Fig. 3. (A) Physiographic map of study area displaying the location of seismic profiles and sediment cores analyzed in this study. SFZ: Shackleton Fracture Zone; OH: Ona High; TB: Terror Bank. (B) Compilation of sediment cores reported in the southern Drake Passage-Scotia Sea region. Referenced sites: ODP 1098 (Domack et al., 2001); GC02, GC03 and NCS09 (Yoon et al., 2002); GC05-DP02 (Lee et al., 2012); GC98–06 (Yoon et al., 2009); GC03-C1, GC03-C2, GC03-C4 and GC04-G03 (Kim et al., 2018; Shin et al., 2020); GC02-SS01 and GC02-SS02 (Yoon et al., 2007; Kim et al., 2018); GC02-SOI03 (Lee et al., 2010); PS67/197–1 and PS67/219–1 (Xiao et al., 2016); MD07–3133 and MD07–3134 (Weber et al., 2012); ODP 696, ODP 695 and ODP 697 (Barker et al., 1988) and U1536, U1537 and U1538 (Weber et al., 2019).

(Poland), where ^{14}C concentration was measured with a Compact Carbon AMS spectrometer (Goslar et al., 2004). All ^{14}C ages were calibrated into calendar years Before Present (BP) using CALIB Radiocarbon Calibration Program 8.1.0 (Stuiver et al., 2020) and the MARINE20 calibration curve (Heaton et al., 2020) (Table 1). As proposed for the Antarctic Peninsula-Scotia Sea region in previous studies (e.g., Domack et al., 2001; Pugh et al., 2009; Xiao et al., 2016, and references therein), we have considered a constant reservoir age of 1300 years ($\Delta R = 900$ years) in all samples. The available age data do not provide high enough resolution to capture intra-Holocene millennial-scale climatic variability, but enable the broad distinction between glacial and deglaciation regimes, as reported in diverse settings around Antarctica (e.g., Yoon et al., 2009; Lee et al., 2012; Xiao et al., 2016; Kim et al., 2020).

3.3. Sedimentological analysis

Sedimentary units naming convention for this study uses a top-down unit labeling according to IODP standards in the Scotia Sea (Weber et al., 2021). Sedimentary units were defined on the basis of visual core descriptions and sediment composition analysis (e.g., Tucker, 2001). Textural classification of Folk (1954) was applied. Macroscopic visual core observations were aided by high-resolution digital images obtained from archive halves using a CoreScan II imaging device coupled to a GEOTEK Multi-Sensor Core Logger (MSCL 81) at the Spanish Geological Survey (IGME, Spain). Sediment characterization included lithology, grain size, sediment texture and structure and bioturbation intensity. The relative composition of biogenic and terrigenous grains, grain size and shape were determined microscopically using a binocular microscope and a high-resolution field emission scanning electron microscope (FESEM). Secondary electron (SE) and back-scattered electron (BSE) imaging were obtained with a GEMINI (FESEM) CARL ZEISS microscope at the Scientific Instrumentation Center (CIC, University of Granada, Spain), equipped with an energy-dispersive X-ray spectroscopy system (EDX).

3.4. Physical and geochemical properties

Physical properties (magnetic susceptibility, gamma-ray density, electrical resistivity and P-wave velocity) were determined at 1-cm resolution on split core surfaces of the archive halves using a GEOTEK Multi-Sensor Core Logger (MSCL) 81 at the Spanish Geological Survey (IGME, Spain).

Major element compositions were measured on core surfaces of the archive halves at 1-cm interval resolution, using a MSCL-X-ray fluorescence (XRF) Core Scanner at the Spanish Geological Survey (IGME, Spain). All core sections were scanned at 10 kV for Al, Si, K, Ca, Ti, Mn, S and 30 kV for Br, Zr and Rb. XRF spectra were processed with bAxil software (next generation version of WinAxil) and include spectrum smoothing and background subtraction, sum peaks and escape peak correction and deconvolution and integration of peaks. These data are provided as element intensities in total counts per second (cps), which are relative to the real chemical concentration of the measured elements (e.g., Weltje and Tjallingii, 2008, and references therein). For the present study, we only report on the following elements and elemental ratios: Aluminum (Al), Silica (Si), Potassium (K), Titanium (Ti), and Bromine (Br), and K/Ti and Br/Ti). Elemental counts of Si, K, and Al, commonly used as detrital proxies (e.g., Rothwell and Croudace, 2015, and references therein), have been plotted against the lithological logs to assess variations in the influx of terrigenous materials to the study sites. K/Ti ratios are sensitive to glacial/interglacial fluctuations (Bertram et al., 2018), as variations in K/Ti ratios indicate the provenance of terrigenous materials (e.g., Monien et al., 2012; Bertram et al., 2018) and are related with the amount of mica and illite phyllosilicates present (e.g., Diekmann et al., 2008). Furthermore, Br/Ti ratios have been previously used as indicators of organic matter in sediments and of paleoproductivity (Agnihotri et al., 2008; Bahr et al., 2014; Salabarnada et al., 2018; Evangelinos et al., 2020).

3.5. Diatom abundance and assemblages

To study diatom abundance and assemblages, cores TG-01 and TG-03 were sub-sampled at 10–20 cm intervals, with a total of 25 samples analyzed in each core (see Supplementary Tables 1 and 2 for details). Quantitative diatom slides were prepared by a random settling method (Warnock and Scherer, 2014). Permanent glass slides were mounted in Norland Optical Adhesive 61 and cured under an ultraviolet light. Slides were examined under Olympus CX31, BX60 and Zeiss Primo Star light microscopes at Colgate University (USA), using a 100× oil immersion objective for a total magnification of 1000×. A minimum of 400 diatom valves (when >50% of the valve is present) were counted along transects, except when diatom absolute abundance was very low. In those instances, ten transects were counted, as has been done with other diatom-poor sediment samples (Rebesco et al., 2014; Holder et al., 2020; Spaulding et al., 2020). These counts include *Chaetoceros*, since their abundance was not overwhelming, as often occurs in sediments from the western side of the Antarctic Peninsula, where both total counts, as done here, and '*Chaetoceros*-free' counts, not done here, necessary. Diatoms were identified to species level whenever possible (e.g., Armand et al., 2005; Cefarelli et al., 2010).

3.6. Regional sediment core comparison

Similar lithologies, magnetic susceptibility (MS) and diatom abundance data analyzed in cores TG-01 and TG-03 enabled the comparison with other Drake Passage-Scotia Sea sediment core records spanning the late Pleistocene-early Holocene. Although strata correlations over long distances involve uncertainties, the comparison of sediment cores is attempted in order to place the observations in a regional context and to highlight distinctive paleoceanographic and paleoenvironmental patterns. The data presented in this paper from cores TG-01 and TG-03 are compared with data from ODP Site 1098 from Palmer Deep (Barker et al., 1999; Domack et al., 2001; Sjunneskog and Taylor, 2002), GC98–06 core from Phoenix region (Yoon et al., 2009), GC02-SS01 core from Protector Basin (Yoon et al., 2007; Bak et al., 2007), PS67/219–1

Table 1
Acid insoluble organic matter radiocarbon dates from sediment cores TG-01 and TG-03. The CALIB 8.1.0 software (Stuiver et al., 2020) and the MARINE20 dataset (Heaton et al., 2020) were used to convert the ^{14}C ages to calendar ages with 2σ precision, applying a reservoir correction of 1300 years ($\Delta R = 900$ years) following Domack et al. (2001), Pugh et al. (2009) and Xiao et al. (2016).

Core	Core depth (cm)	Uncorrected age (^{14}C yr BP)	Error (± yr)	Corrected and calibrated age (2σ) (cal. yr BP)		
				Lower cal. range	Upper cal. range	Median probability
TG-01	10	13,120	70	13,349	13,773	13,562
TG-01	230	21,830	140	23,781	24,560	24,148
TG-01	270	22,140	150	24,097	24,972	24,527
TG-03	15	11,600	60	11,607	12,177	11,882
TG-03	210	22,710	160	24,779	25,624	25,202

core from Pirie Basin (Xiao et al., 2016), and PS67/197–1 core from the Central Scotia Sea (Xiao et al., 2016) (Fig. 3B).

4. Results

4.1. High-resolution seismic stratigraphy

Four seismic units named U4 to U1 from older to younger have been identified in Ona Basin (Fig. 4). Seismic facies mostly exhibit parallel to subparallel or wavy stratified configurations (Fig. 4C), with relatively high acoustic amplitudes and high lateral continuity along the basin floor on both sides of Ona High (e.g., Fig. 5). The seismic units have erosional limits at the margins of the basin floor, often related with transparent, irregular-to lens-shaped acoustic facies with no internal reflections (Fig. 4C) that become conformable through the rest of the basin floor. The most recent sedimentary cover (i.e., units U2 and U1) is relatively thick above the western side of Ona High and the entire basin floor in both sub-basins; in contrast, it is thin or absent above the eastern and northern Ona High, southwestern Terror Bank and the offshore slopes of Elephant Island (Fig. 5).

Seismic units U4 and U3 have two main depocenters, located on the proximal western Ona sub-basin and on the distal eastern Ona sub-basin. Seismic unit U4 shows a maximum thickness of about 40 ms, whereas the maximum thickness of unit U3 is up to 35 ms (Fig. 4C).

The present-day mounded and sheeted topography of the western and eastern Ona sub-basins (e.g., see Fig. 7 in López-Quirós et al., 2020), is generated by seismic units U2 and U1. These units exhibit major changes in the distribution pattern, with thickness increasing progressively towards the basin floor in both sub-basins (Fig. 5). Patchy distributions are found in the proximal slope of the basin and over structural highs such as Ona High, associated with lens-shaped or irregular bodies with transparent acoustic facies (Figs. 4C and 5). Seismic units U2 and U1, which exhibit similar average thickness of about 20 ms, are separated by a seismic discontinuity that marks an internal increase in acoustic amplitude, laterally correlated through the entire basin floor (Fig. 4A-C). Likewise, a minor internal discontinuity within the most recent unit U1 was depicted based on core-seismic correlation (Fig. 4B; see discussion below).

4.2. AMS ^{14}C dating

The calibrated ^{14}C ages decrease from bottom to top from 24,527 yr BP at 2.7 m depth, 24,148 yr BP at 2.3 m depth, and 13,562 yr BP at 0.1 m depth in core TG-01, and from 25,202 yr BP at 2.1 m depth, and 11,882 yr BP at 0.15 m depth in core TG-03 (Table 1). Accordingly, ^{14}C results suggest deposition during the LGM and its subsequent deglaciation, with average sedimentation rates of 13 and 14.6 cm/kyr from cores TG-01 and TG-03, respectively.

4.3. Sedimentary units

Four sedimentary units have been defined from the core bottom upward: IV, III, II, and I (Fig. 6).

4.3.1. Unit IV: diatom-rich mud and silty mud

The lowermost Unit IV is comprised of slightly bioturbated diatom-rich mud and silty mud with sparse ice-rafted debris (IRDs), mostly composed of granules and coarse sands (Fig. 6). Coarse-grained intervals also were observed at the base of small turbidite events (Fig. 7A). In addition, SEM observations indicate that those coarse-grained intervals are well sorted (Fig. 8A). Magnetic susceptibility (MS) and density values are high and fluctuate considerably, while greater variability characterizes core TG-01 (Fig. 6). These values show an inverse relationship with diatom abundances (Fig. 6). Terrigenous elements (Si, K, Al) and K/Ti ratio in TG-01 exhibit a bottom-up increasing trend up to 3.45 m depth, followed by a general decreasing trend towards the top of Unit IV (Fig. 6A). Br/Ti ratio fluctuates considerably, with high values at 3.8 m and 3.5–3.7 m depths (Fig. 6A). In TG-03 terrigenous elements and K/Ti ratio follow a bottom-up increasing trend, while Br/Ti ratio show no significant variability (Fig. 6B).

4.3.2. Unit III: IRD-rich, gravelly silty/sandy mud

Unit III is composed of gravelly silty to sandy mud with large amounts of IRDs including dropstones (Figs. 6 and 7B–E). IRD is scattered but also concentrated in patches (Fig. 7D and E). Bioturbated silty to sandy muds were also observed in core TG-01 (Figs. 6A and 7D). MS and density values are high and fluctuating in core TG-01 (Fig. 6A), coincident with large amounts of IRDs and isolated dropstones (Figs. 6A and 7C). A general bottom-up decrease is observed in core TG-03 (Fig. 6B). Moreover, MS and density values exhibit roughly inverse relationships with diatom abundances (Fig. 6). SEM analyses indicate that Unit III sediments are moderately to well sorted (Fig. 8B and C). SEM observations also indicated a clay fraction mostly dominated by illite (see a detailed view of ragged/compacted illite plates in Fig. 8B). In TG-01, terrigenous elements and K/Ti ratio display a bottom-up increasing trend up to 3 m depth, followed by a decreasing trend towards the top of Unit III (Fig. 6A). Br/Ti ratio in Unit III at TG-03 exhibits minimum values, with a short peak at 2.2 m depth (Fig. 6A). Terrigenous elements and K/Ti ratio in TG-03 exhibit bottom-up increased values, characterized by an increasing up to 1.85 m depth, followed by a decreasing trend towards the top of the unit. In contrast, Br/Ti ratio remains invariant (Fig. 6B).

4.3.3. Unit II: bioturbated diatomaceous mud

Unit II mostly consists of bioturbated diatomaceous mud (Fig. 6) with intercalations of sparse bands and/or layers composed of increased amounts of well-preserved diatom assemblages (Fig. 8D-F; also see peaks in diatom abundance: Fig. 6). The diatomaceous mud is affected by intense bioturbation, generally as a non-descript burrow mottling (Fig. 7F). MS and density values are high but fluctuate considerably with similar bottom-up trends through Unit II, and roughly show inverse relationships with diatom abundances (Fig. 6). SEM observations indicate that Unit II sediments are poorly sorted, while the sand content is very low (e.g., Fig. 8F). However, large amounts of coarse material (mostly fine gravels and coarse sands) are observed in the upper part of Unit II between 0.3 and 0.8 m depths (Fig. 6B) in core TG-03. IRDs are sparse bottom-up and less abundant than in upper and lower units (Fig. 6). SEM observations indicated a clay fraction dominated by illite/smectite (Fig. 8F). Abundant euhedral to sub-spherical authigenic barite grains were observed throughout (Fig. 8G and H), as well as some isolated dropstones (Fig. 7G). In TG-01, terrigenous elements and K/Ti ratio exhibit a bottom-up decreasing trend up to 1.5 m depth, followed by an increasing trend up to 1 m depth. This is followed by a general decreasing trend up towards the top of Unit II (Fig. 6A). Br/Ti ratio displays a decreasing bottom-up trend through Unit II, with their maximum values recorded at the bottom of the unit (Fig. 6A). No significant long-term variations are observed in the terrigenous elements and K/Ti ratio at TG-03. Br/Ti ratio remains also invariant, although maximum values are recorded at the bottom of Unit II (Fig. 6B).

4.3.4. Unit I: diatom-rich silty to sandy mud

Unit I is composed of diatom-rich silty to sandy mud (Figs. 6 and 7H). In core TG-03, Unit I also contains a minor diatomaceous silty mud layer (see peak in diatom abundance: Fig. 6B). Sand content shows a gradual bottom-up increase, while SEM observations indicate a shift in the sorting of the coarse grains from poorly to moderately sorted (Fig. 8I). Moreover, SEM observations display a dominance of illite/smectite in the fine-clay fraction (Fig. 8I). MS and density values exhibit a bottom-up decrease in both cores, with the exception of a peak at 0.02 m in TG-03 (Fig. 6). IRDs are sparse (Fig. 6), although an IRD-rich interval is observed in core TG-01 at the lower part of the unit (Fig. 6A). In core TG-01, terrigenous elements and K/Ti and Br/Ti ratios exhibit a bottom-up

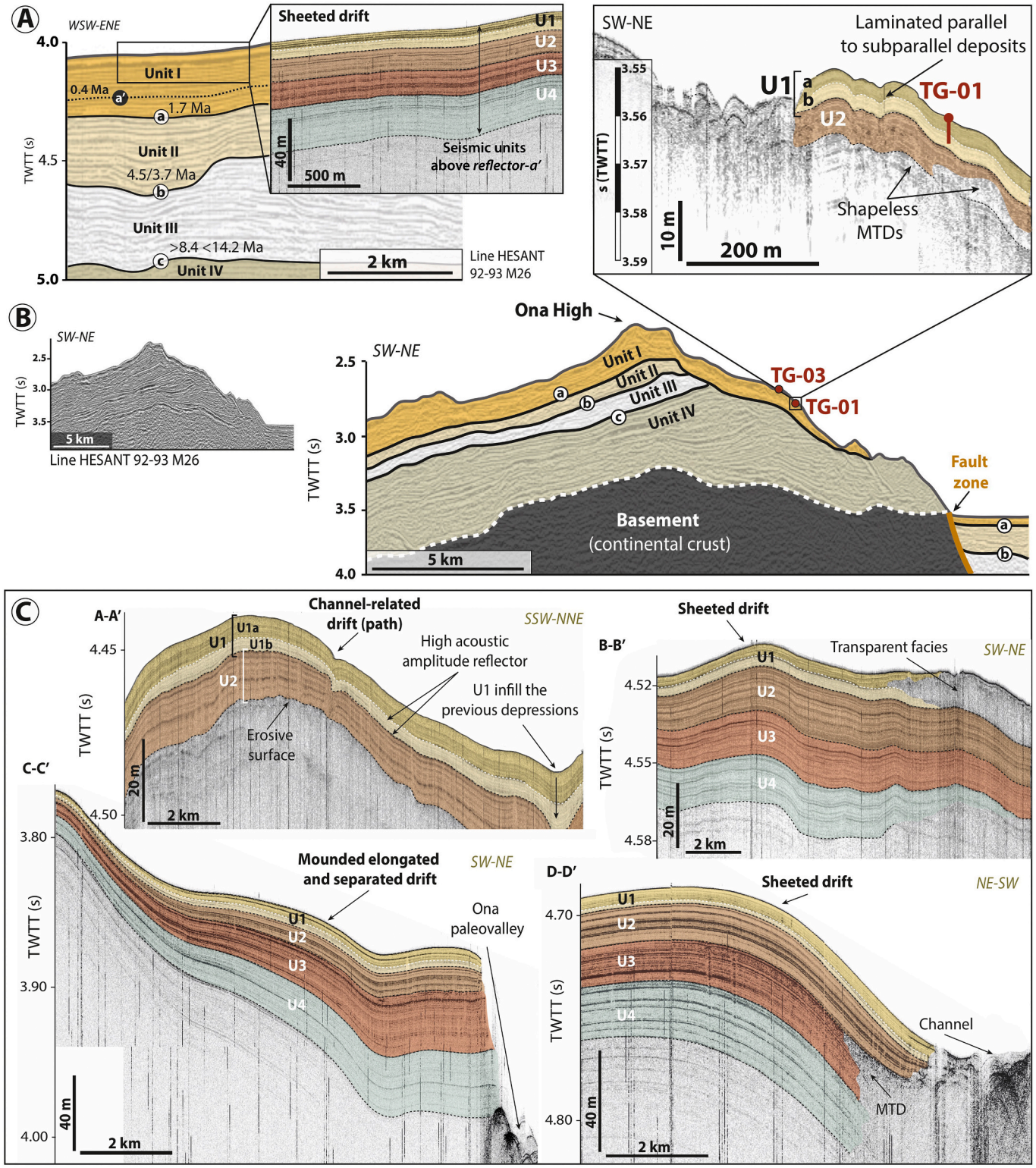

Fig. 4. High-resolution seismic stratigraphic characterization of the southern Ona Basin region. A) Multichannel seismic line HESANT 92–94 M26 from Ona Basin displaying the younger low-resolution (LR) seismic units (Units I to III, above *reflector-c*; Maldonado et al., 2006) and age assessment at a basin scale recently updated by Pérez et al. (2021). For previous age assessments see Fig. 2B. Enlarged squared area corresponds to a projected, parallel TOPAS profile from this study, showing the high-resolution (HR) seismic units U1 to U4. Note that HR seismic units U1 to U4 lie within the younger LR seismic Unit I above *reflector-a'*. Location of HESANT 92–94 M26 segment is shown in Fig. 5. B) Multichannel seismic line across the Ona High, in the vicinity of cores TG-01 and TG-03 (after Maldonado et al., 2006). Note that core TG-03 is projected on that segment. The enlarged area displays the correlation between core TG-01 and a high-resolution sub-bottom profile, allowing the identification of a minor internal discontinuity within the most recent unit U1, subdivided in U1a and U1b. C) Main characteristics of high-resolution seismic units defined in TOPAS profiles. Locations of TOPAS profiles are shown in Fig. 5.

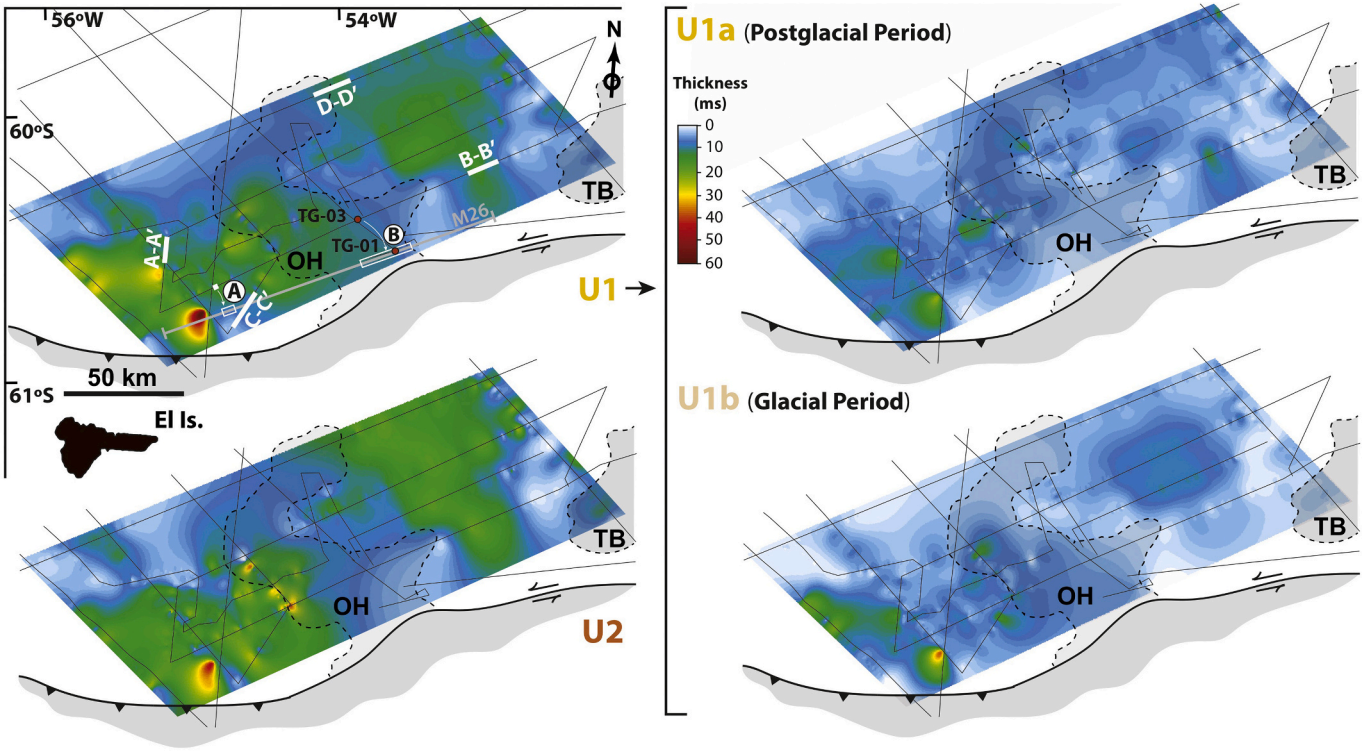

Fig. 5. Isochore maps of the most recent seismic units U1 (subdivided in U1a and U1b) and U2, defined in TOPAS profiles. Note that according to core-seismic correlation (see discussion below), discontinuity within U1 is marking the transition from glacial to postglacial stratigraphy.

increasing trend towards the upper part of the unit (Fig. 6A). A bottom-up increasing trend in terrigenous elements and K/Ti ratio intensities in TG-03 is also observed until 0.15 m depth, followed by a decrease towards the upper part of the unit (Fig. 6B). In contrast, Br/Ti ratio shows an increasing trend up to 0.15 m depth, followed by a decrease until the upper part of the unit (Fig. 6B).

4.4. Bottom-up diatom assemblages

Diatom absolute abundance ranges from ~0.4 to 18 × 10^6 valves/g of sediment in core TG-01, and from ~0.5 to 20 × 10^6 valves/g in core TG-03 (Fig. 6). Diatom abundance is quite variable in Unit IV, (~3–14 × 10^6 valves/g in core TG-01 and ~ 1.5–10 × 10^6 valves/g in core TG-03) (Fig. 6). Diatom abundance decreases sharply through Unit III (~2.5 × 10^6 valves/g), reaching counts of ~0.4 × 10^6 valves/g in core TG-01 and 1.2 × 10^6 valves/g in core TG-03 (Fig. 6). Diatom abundance increases and is generally high through Unit II; at the bottom part of the sedimentary unit, abundance sharply reaches a maximum of ~18 × 10^6 valves/g (Fig. 6). Note however, that the upper part of Unit II (between 0.3 and 0.8 m depth) in core TG-03 has extremely low diatom abundance (Fig. 6B). Br/Ti ratios also increase through Unit II, with higher values recorded coincident with the maximum diatom abundances (Fig. 6). Likewise, abundant authigenic barite grains were observed at the base of Unit II in relation with maximum diatom abundance (Fig. 8G and H). Diatom abundance is almost constant through Unit I (~3 × 10^6 valves/g) in core TG-01 (Fig. 6A); it increases from ~7 to 12 × 10^6 valves/g in core TG-03 (Fig. 6B).

Fragilariopsis kerguelensis (e.g., Fig. 8J) is the most common species in both sediment cores, with total mean abundances of 23–32%, ranging from 3 to 53% (Fig. 9; Supplementary Tables 1 and 2). *Chaetoceros* subg. *Hyalochaete* (referred to as *Hyalochaete*) is also a common contributor in both sediment cores, with total mean abundances of 18% (ranging from 4 to 63%) and 23% (ranging from 0.3 to 70.5%), respectively (Fig. 9; Supplementary Tables 1 and 2). In addition, *Hyalochaete* vegetative valves are more abundant than the resting spores throughout cores TG-01 and TG-03 (Fig. 9). *Eucampia antarctica*, *Thalassiosira lentiginosa* and *Actinocyclus actinochilus* (e.g., Fig. 8J) are subdominant species throughout both sediment cores, with mean absolute abundances of 7% (ranging from 1 to 20%), 5% (ranging from 1 to 8%) and 5% (ranging from 0.4 to 17%) in core TG-01 and 9% (ranging from 3.3 to 18%), 6% (ranging from 1 to 18%) and 4% (ranging from 0.7 to 14%) in core TG-03, respectively (Fig. 9; Supplementary Tables 1 and 2). Less common diatom species include *Thalassiosira antarctica* T2, *Fragilariopsis curta*, *Rhizosolenia* spp. and extinct diatoms (Figs. 8J and 9; Supplementary Tables 1 and 2). A high peak in extinct diatoms, with >40% of reworked species, was observed at 0.5 m depth in core TG-03; the assemblage is composed predominantly by *Denticulopsis* spp., 35%, with most specimens identified as *Denticulopsis simonsenii* (Fig. 9B; Supplementary Table 2).

4.5. Comparison of different regional sediment cores: sedimentation patterns

Comparison of cores TG-01 and TG-03 with other Drake Passage-Scotia Sea records (Fig. 10) shows common sedimentation patterns, with detrital materials deposited preferentially during glacial conditions, in contrast to hemipelagic sedimentation with an abundant biogenic fraction accumulated during interglacials. In general, glacial deposition shows a progressive increase from west (Drake Passage) to east (Central Scotia Sea), with 1–2 m thick deposits in the study area (southern Ona Basin). The record of the postglacial period (including the deglaciation) also seems to be more condensed in the study area (less than 2 m thick) than in most settings of the Scotia Sea (up to 3 m thick) (Fig. 10).

5. Discussion

5.1. Considerations about radiocarbon dating

Radiocarbon dates obtained near the core tops (13,562 yr BP and

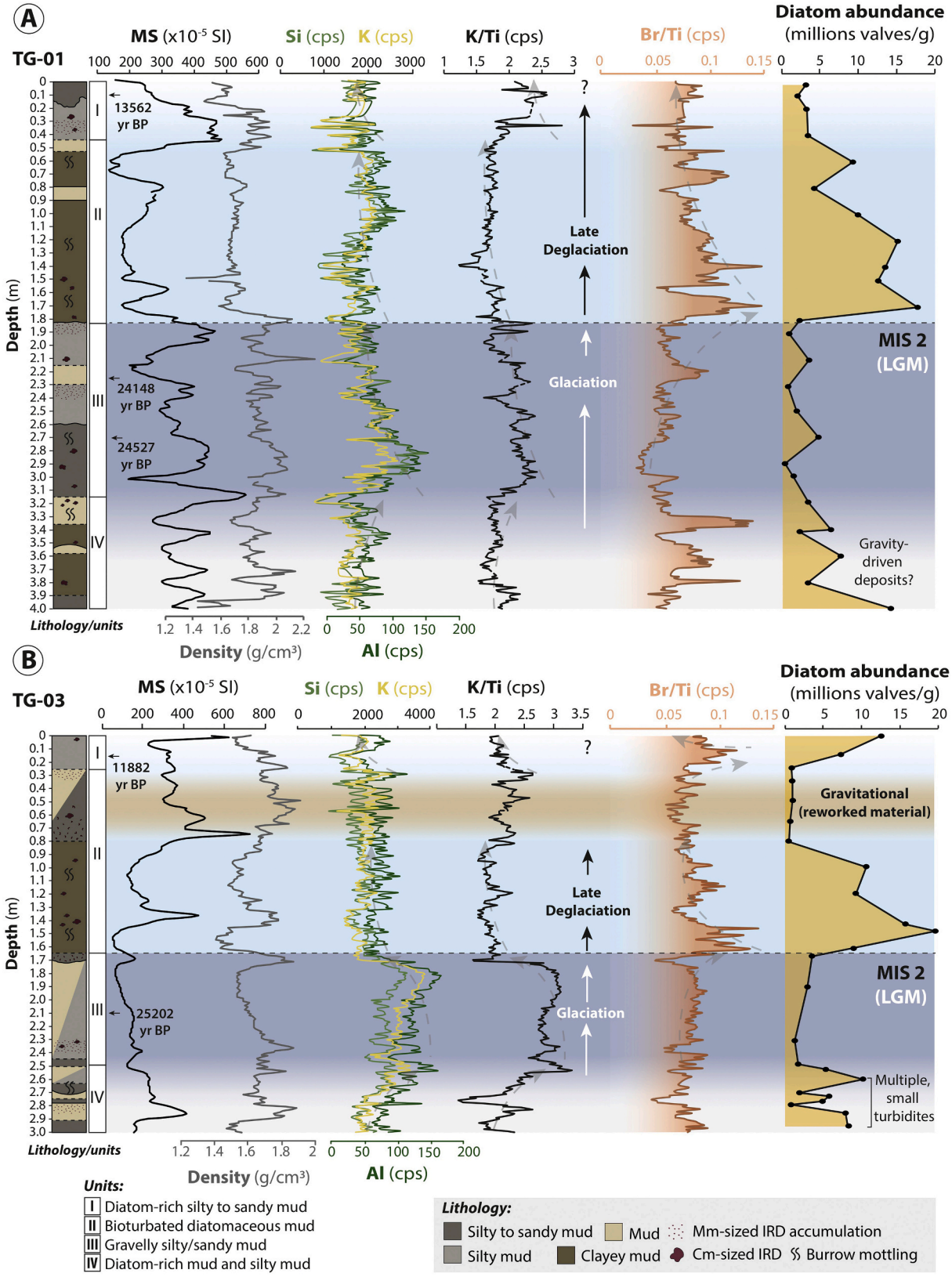

Fig. 6. A) and B) Graphic lithological logs with measured radiocarbon ages (^{14}C yr BP), and bottom-up variations in magnetic susceptibility (MS x10^{-5} SI), density (g/cm^3), XRF-scan data (i.e., variations in terrigenous elements (Si, K, Al) and K/Ti and Br/Ti ratios) and diatom absolute abundances in sediment cores TG01 and TG03.

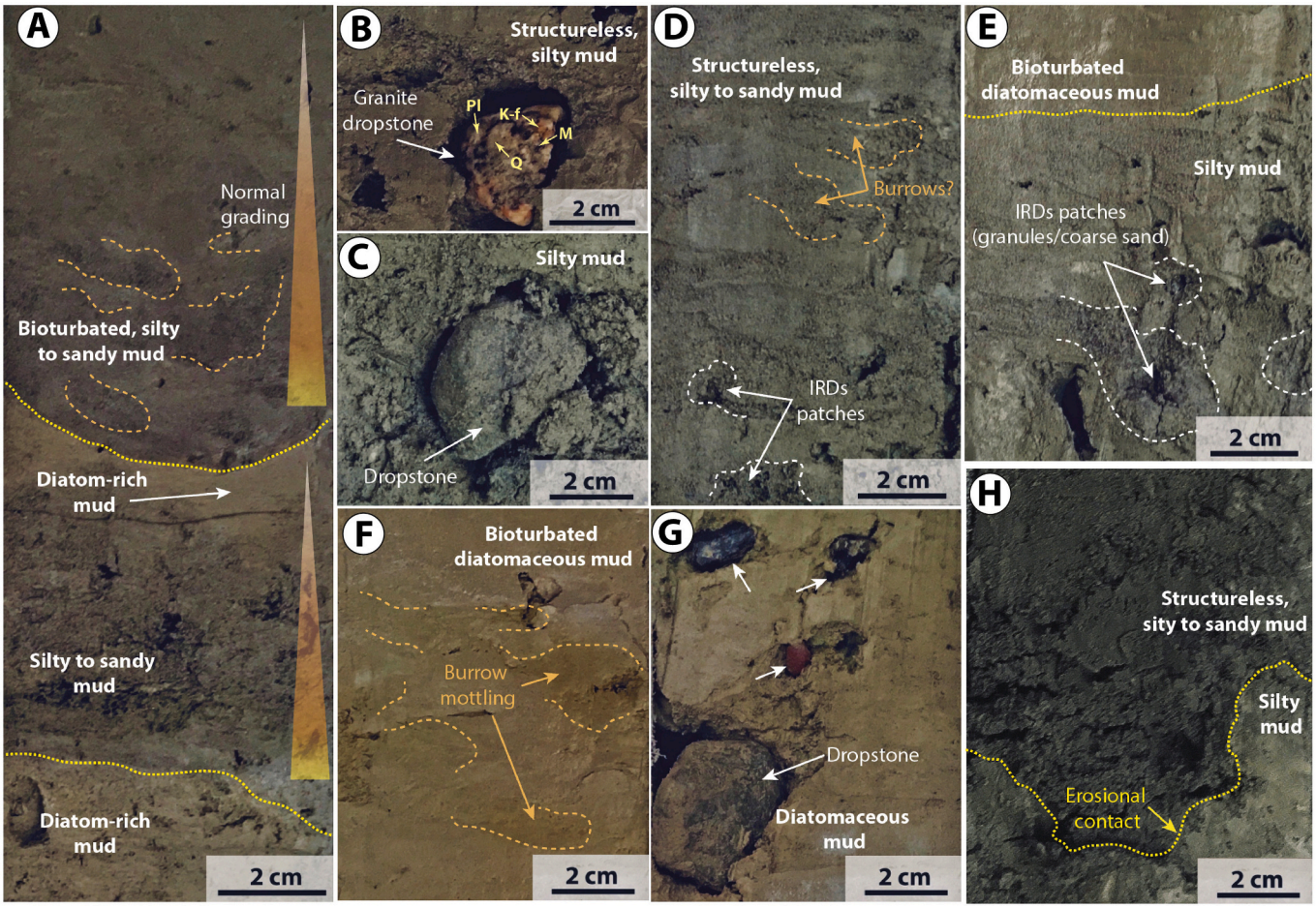

Fig. 7. Detailed facies characterization of sedimentary units identified in cores TG-01 and TG-03. A) Core slab example of Unit IV (diatom-rich mud and silty mud; core TG-03) exhibiting fining-upward small turbidites. B) and C) Core slab examples of Unit III (gravelly silty mud; cores TG-03 and TG-01, respectively) displaying large sub-rounded dropstones up to 4 cm in diameter, including a granite rock fragment. D) Core slab example of Unit III (gravelly silty/sandy mud; core TG-01) showing both IRD patches and vaguely expressed burrowing activity. E) Core slab example of the transition between Units II and Unit III (i.e., from bioturbated diatomaceous to gravelly silty mud; core TG-01). IRD patches are observed in Unit III. F) Core slab example of Unit II (bioturbated diatomaceous mud; core TG-03) displaying burrow mottling texture. G) Core slab example of Unit II (bioturbated diatomaceous mud; core TG-03) showing sub-rounded to rounded dropstones ranging in size from 1 to ~3 cm. H) Core slab example of Unit I (diatom-rich silty to sandy mud; core TG-01) showing a sharp, erosional contact between silty and sandy mud.

11,882 yr BP, respectively) are considerably older than the reservoir age of 1300 years for the Antarctic Peninsula and Scotia Sea region (e.g., Domack et al., 2001; Pugh et al., 2009; Xiao et al., 2016). However, these age values are in agreement with regional age data. For example, core GC03-C1 located 50 km away from our study sites (Fig. 3B) shows similar radiocarbon dates near the core top (12,290 yr BP; Shin et al., 2020). Additionally, these authors recovered a box core (BC03-C1) with a core top ^{14}C age of 4037 yr BP (Shin et al., 2020). After calibration using BC03-C1, a final core top age of 8790 yr BP was proposed for GC03-C1, which is also older than the reservoir age used for the study area (e.g., Xiao et al., 2016). Other surficial ages measured in the region range between 12,864 ± 60 yr BP in the southern Drake Passage (Yoon et al., 2009) and 6000 yr BP in the Weddell Sea (Pudsey and Evans, 2001).

Old AMS ^{14}C ages of Antarctic surface sediment cores have been related to contamination by old carbon (Gordon and Harkness, 1992), triggered either by the release of carbon dioxide preserved in ice sheets (e.g., Domack et al., 1989), along with the uptake of dissolved inorganic carbon by recycled ancient organic matter (e.g., Andrews et al., 1999; Gibson et al., 1999). Consequently, the near surface ages of the study area may be related to contamination by reworked old organic matter transported by strong bottom currents and/or by gravitational processes. Indeed, the southern Ona Basin is affected by a vigorous westward-flowing WSDW along the continental slope (Naveira Garabato et al., 2002a, 2002b; Legg et al., 2009). Also, deep-water downslope processes are enhanced by the topographic obstacle of the Ona High, that has undergone a widespread dismantling leading to ubiquitous mass transport deposits (MTDs) generation (López-Quirós et al., 2020). Alternatively, the absence of consistently low magnetic susceptibility values at the core tops (Fig. 6) would support the occurrence of sediment loss during coring operations, as discussed in other settings of the Scotia Sea (Xiao et al., 2016). The available data do not permit discrimination between these two possibilities, and both are likely contributors. Core-top losses during coring operations is always a possibility, especially during gravity and piston coring, as opposed to box and multi-coring activities. Without complementary collection of cores that would have enabled a more reliable recovery of the sediment-water interface, the determination of the amount of core top losses is not possible. However, radiocarbon data do support the interpretation of a post-Last Glacial Maximum age of the uppermost sediment unit. In addition, the increased diatom contents, along with the decreased contribution of reworked diatoms, supports the deglacial to Holocene age of this unit.

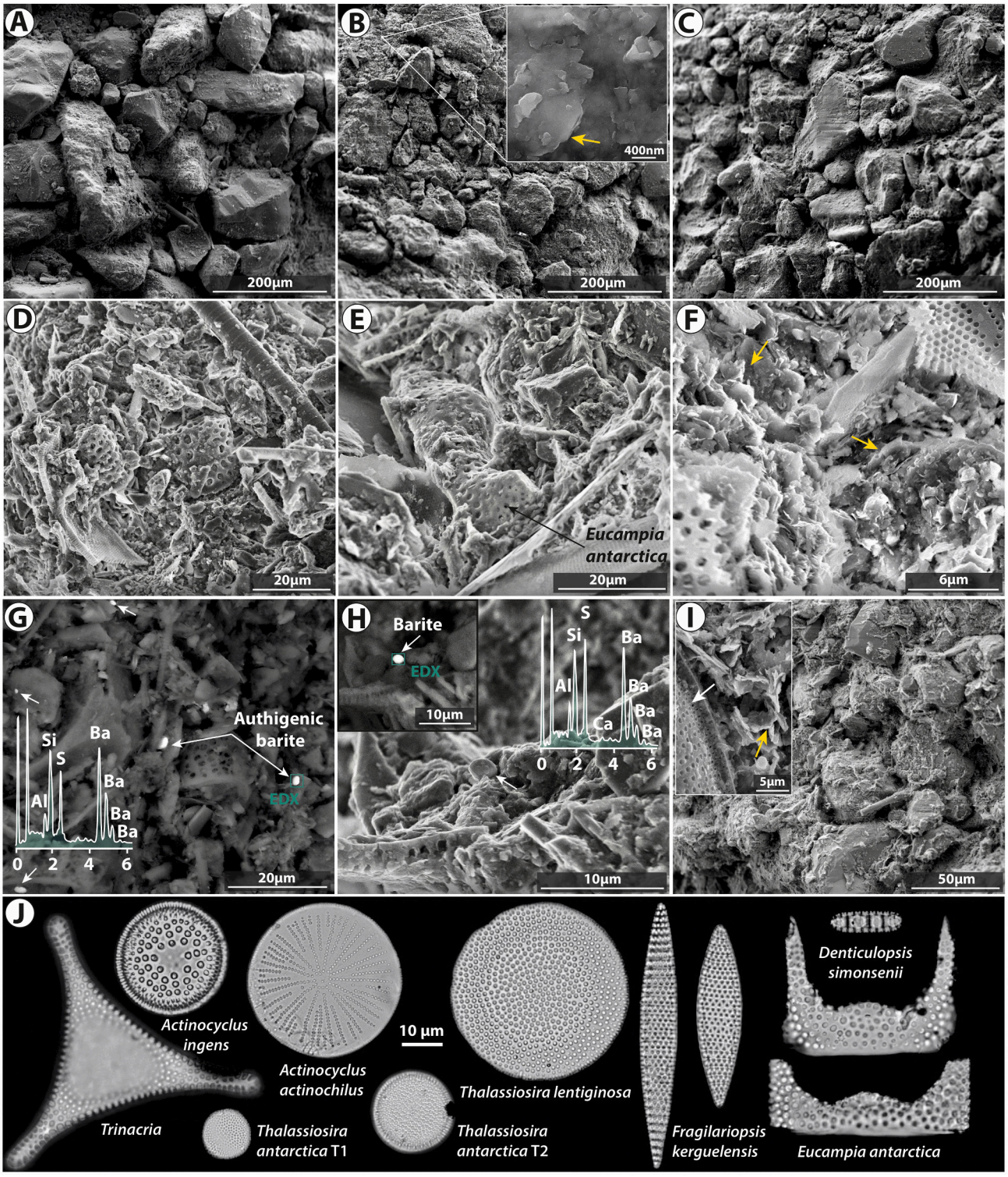

Fig. 8. Sedimentation at the studied cores TG-01 and TG-03. A) SEM (BSE) photomicrograph of Unit IV (core TG-03) showing coarse grains deposited at the base of a turbidite. B) and C) SEM photomicrographs (SE) of Unit III (core TG-01) showing moderately to well-sorted, silty to sandy mud. Enlarged area in B) displays the clay fraction dominated by ragged and compacted illite plates (yellow arrow). D), E) and F) SEM photomicrographs (SE) of Unit II (cores TG-01, TG-01 and TG-03, respectively) showing diatom-rich, diatomaceous mud. Yellow arrows indicate illite/smectite clays. G) and H) SEM (BSE) photomicrographs and related energy-dispersive X-ray (EDX) analysis of sub-spherical barite grains (white arrows) observed in Unit II (cores TG-03 and TG-01, respectively). Note that the corresponding SEM (SE) photomicrograph is also exhibited in H) for a detailed textural description. I) SEM photomicrograph (SE) of Unit I (core TG-01) displaying silt and clay fractions of moderately sorted, diatom-rich silty mud. Squared area in the upper-left corner shows the clay-sized matrix dominated by illite/smectite (yellow arrow) and diatoms (white arrow). J) Plane-polarized light photomicrographs of different diatom assemblages identified in this study. (For interpretation of the references to colour in this figure legend, the reader is referred to the web version of this article.)

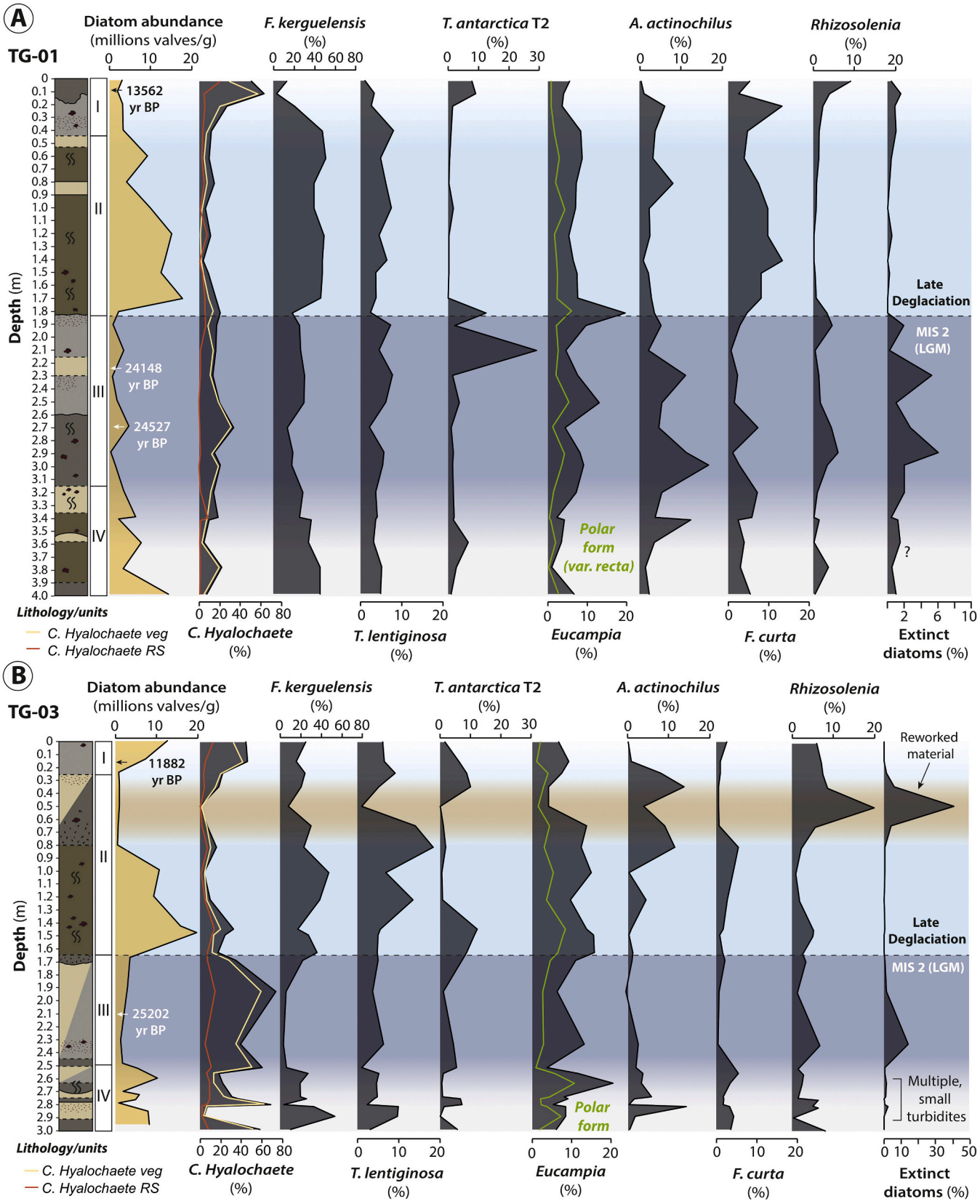

Fig. 9. A) and B) Bottom-up variations of selected diatom assemblages in cores TG01 and TG03, respectively. For complete diatom assemblage information see Supplementary Tables 1 and 2. Note that *Chaetoceros* subg. *Hyalochaete* is also plotted as vegetative valves (yellow) vs. resting spores (orange). (For interpretation of the references to colour in this figure legend, the reader is referred to the web version of this article.)

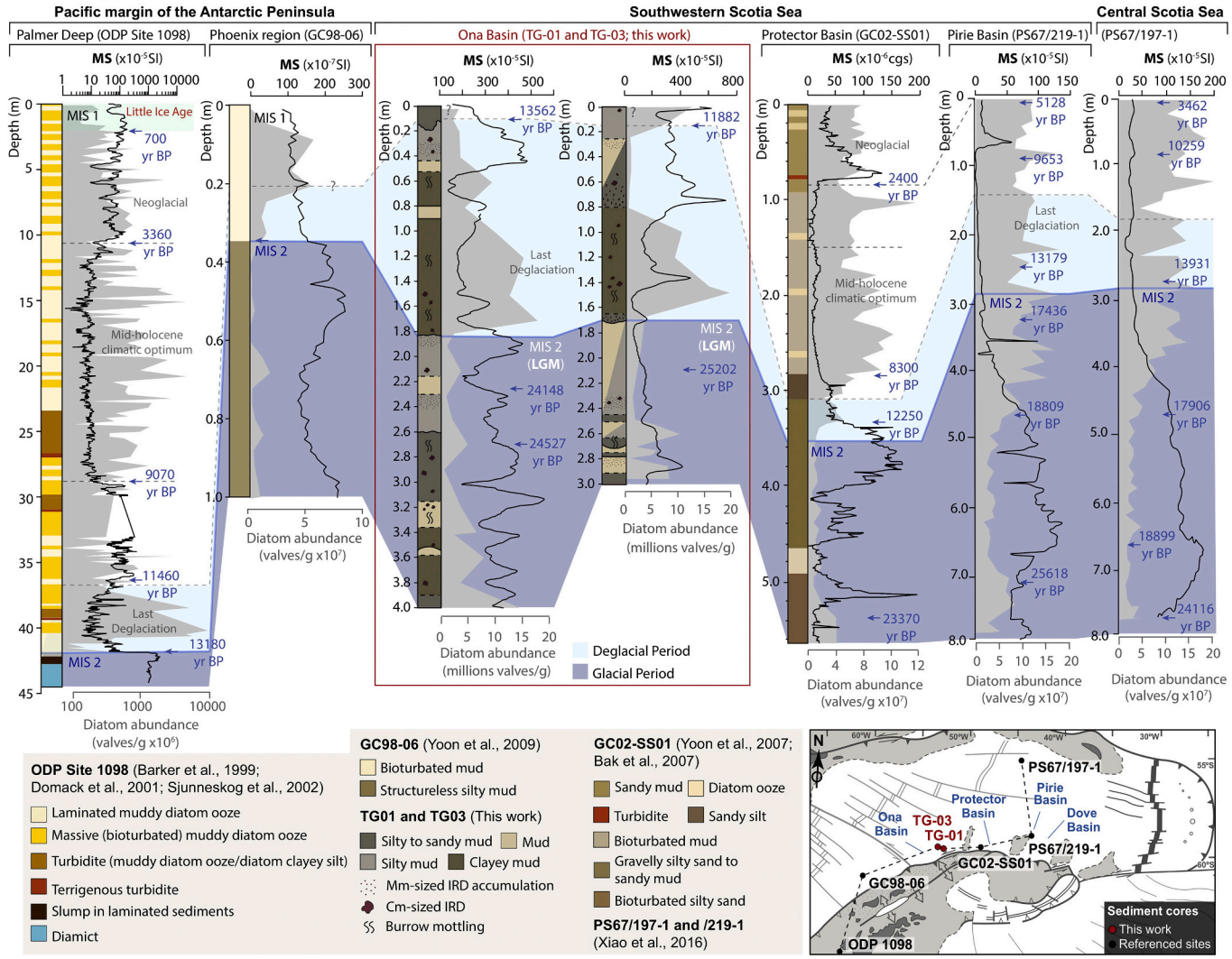

Fig. 10. Core-to-core comparison transect across the Drake Passage-Scotia Sea, including cores TG-01 and TG-03 analyzed in this work. Note that glacial and deglacial periods are highlighted across the core-to-core comparison. Referenced sites: ODP 1098 (Barker et al., 1999; Domack et al., 2001; Sjunneskog and Taylor, 2002); GC98–06 (Yoon et al., 2009); GC02-SS01 (Yoon et al., 2007; Bak et al., 2007); and PS67/219–1 and PS67/197–1 (Xiao et al., 2016). LGM: Last Glacial Maximum.

5.2. *The record of glacial-interglacial variability*

5.2.1. *Late Quaternary sedimentary evolution*

The four high-resolution (HR) seismic units defined in this work lie within the most recent low-resolution (LR) seismic Unit I above *reflector-a* (Fig. 4A) (Maldonado et al., 2006, 2014; Pérez et al., 2019). Updated age models from IODP Expedition 382 frame LR Unit I from the Middle Pleistocene (i.e., 1.7 Ma) to the recent (Pérez et al., 2021; Figs. 2A and 4A). LR Unit I exhibits a relatively thin (maximum thickness of 0.6 s in the study area) and continuous sheet-like geometry, incised by channels and moats in many places and with small amplitude sediment waves towards the top of the unit (Pérez et al., 2019). Within LR Unit I, a minor internal discontinuity referred to as *reflector-a'* (see Fig. 2B) was originally documented in the nearby Dove and Pirie basins (Pérez et al., 2017), and later recognized in the western Ona High (Pérez et al., 2019) (also Fig. 2B). *Reflector-a'* has been dated at 0.7 and 0.4 Ma (Pérez et al., 2021), and its genesis has been related to the collapse of the West Antarctic Ice Sheet (WAIS) with reduced input from East Antarctica (e.g., Raymo and Mitrovica, 2012; Wilson et al., 2018), when global sea level was higher that present-day sea level (e.g., Raymo and Mitrovica, 2012).

HR units with similar facies and thickness distribution have also been reported in the most recent sedimentary record of Scan Basin (Fig. 1), where they constitute the upper part of a low-resolution unit of tentative late Pliocene to Quaternary age (García et al., 2016). Since the HR units defined in this study are deposited above *reflector-a'*, a late Quaternary age is most likely for those units. Previous high-resolution seismic studies in glacial environments have documented periodic alternations of depositional environments driven by glacial cycles, for example, the Chukchi Margin, Arctic Ocean (Kim et al., 2021). These glacial cycles also have been recorded by a diversity of proxies in the Scotia Sea (Xiao et al., 2016). In this sense, we deduce that HR unit generation is primarily dictated by the late Quaternary glacial-interglacial cyclicity, as the timing from *reflector-a'* to the present encompasses several glacial-interglacial cycles.

In nearby Scotia Sea basins (i.e., Pirie and Dove basins; Weber et al., 2021; Pérez et al., 2021), the fast growth of contourite drifts from the Mid-Pleistocene to the present has been associated with enhanced Southeast Pacific Deep Water (SPDW) flow due to enhanced Pacific Overturning Circulation (Kwiek and Ravelo, 1999). In contrast, the contributions of sediment transport from the Antarctic continental shelf are considered to have been low (Pérez et al., 2021). In agreement with

these considerations, the formation of LR Unit I in Ona Basin is interpreted to be connected with the onset of the modern oceanic circulation pattern in the Scotia Sea (Pérez et al., 2019). The recognition of high-resolution stratigraphies in contourite deposits in the Scotia Sea are considered as indicative of bottom flow variations through Pleistocene glaciations (e.g., Owen et al., 2014). Likewise, the marked increase in seismic amplitude and erosional character of the depositional style noticed between the older HR U4 and U3 units and the younger HR U2 and U1 units (Fig. 4C) are interpreted as the effect of major fluctuations in the regional bottom-current patterns, as documented in the Scan Basin (García et al., 2016). Furthermore, the spatial arrangement of contourite deposits in the southern margin of the Ona Basin revealed significant changes along the westward path of the WSDW bottom current (López-Quirós et al., 2020). In the eastern sub-basin, slope-plastered and sheeted drifts (e.g., Fig. 4C, profile B-B′) indicate low-velocity currents flowing mostly as simple, tabular water masses. Westward, mounded elongated drifts (e.g., Fig. 4C, profile C-C′) indicate higher-energy environments (e.g., Stow et al., 2008) and suggest a westward increasing bottom current. Consequently, the seafloor morphology points to an intensification of the westward WSDW in the southern basin, as previously reported by López-Quirós et al. (2020).

In addition to bottom current activity, during deposition of each unit the recognition of transparent bodies would indicate the formation of MTDs, signaling the interaction between along- and downslope processes during successive glacial cycles (Fig. 4C). The co-occurrence of stratified and chaotic facies has also been documented in other high-latitude settings, such as the central Arctic Ocean, where phases of MTD development have been related mainly with glacial erosion processes (Pérez et al., 2020) and with their changing influence thorough successive late Quaternary glacial cycles (Kim et al., 2021). In contrast to those settings, in the study area the overall along-slope orientation of morphological features (López-Quirós et al., 2020) indicates that the sediment load delivered to the southern margin of the basin is mainly reworked by the action of bottom currents and incorporated in the contourite drifts (Fig. 4C). Thus, generation of MTDs would probably be coeval and secondary to contourite deposit formation, as evidenced in other glacial margins where drift sediments act as a precondition factor for subsequent development of mass movements (Baeten et al., 2016; Osti et al., 2019). This pattern contrasts with other Antarctic settings, where along- and downslope processes alternate temporally (e.g., Presti et al., 2011). In Ona Basin, the interaction has persisted to the present-day situation, as reflected in the basin geomorphology (López-Quirós et al., 2020). Such recent interactions have been documented in specific sectors of the margins around the Scotia Sea (Pudsey and Howe, 2002; Owen et al., 2014).

We infer that HR units U4 to U3 possibly were deposited during a generally high production and outflow of WSDW through the Scotia Sea, where both WSDW and energetic ACC flows would have been sustained by a dynamic Atlantic Meridional Overturning Circulation (AMOC) during Marine Isotope Stage (MIS) 11 at ~0.4 Ma (Doherty and Thibodeau, 2018). During the formation of HR U4 and U3 units, the westward flow of the WSDW would have affected the entire southern margin of the Ona Basin, being less vigorous and consequently limiting important erosion and subsequent deposition.

Conversely, younger HR U2 and U1 units likely reflect intensifications in the bottom-current flows, probably due to latitudinal displacements of the interphase between the deeper part of the ACC (i.e., the CDW) and the WSDW that enhanced the erosional capacity of the westward flow. The spatial variability of the ACC fronts in the southern Ona Basin could have influenced a southward extension of CDW farther south, as documented in the nearby Drake Passage (Wu et al., 2019). The enhanced influence of the CDW and ACC-related fronts in comparison with eastern Scotia Sea basins has been related to the low confinement of Ona Basin (López-Quirós et al., 2020).

5.2.2. *Late Pleistocene-early Holocene sedimentary processes*

Radiocarbon dates for cores TG-01 and TG-03 indicate that sedimentary units with high magnetic susceptibility and density values, high occurrence of IRDs, and low diatom absolute abundance and Br/Ti ratios correspond to the LGM (see below) (Fig. 6), whereas the units consisting of low magnetic susceptibility and density values, and higher biogenic content inferred from high diatom absolute abundance and Br/Ti ratios, correspond to the Last Deglaciation (see below) (Fig. 6). Moreover, mean sedimentation rates of 13 and 14.6 cm/kyr are comparable to rates (<13.5 cm/kyr) estimated in the continental rise west of the Antarctic Peninsula (Pudsey, 2000). Consequently, as a first approximation, our study sites cover the late Pleistocene paleoceanographic history (i.e., the most recent time during the Last Glacial Period).

5.2.2.1. The Last Glacial Maximum. The LGM was characterized by extensive sea ice and ice shelf advancement, with seafloor ice grounding reported in the Weddell Sea and the Antarctic Peninsula Shelf (e.g., Pudsey et al., 1988; Anderson et al., 1991; Gersonde et al., 2005; Collins et al., 2012; Bak et al., 2014; Bentley et al., 2014; Xiao et al., 2016; Kim et al., 2018, 2020; Shin et al., 2020). Sea ice expansion was allowed by the northward retreat of the oceanic fronts, which also resulted in a reduced influence of the ACC in the southern Scotia Sea (Pudsey et al., 1988; Kim et al., 2020). The grounded ice sheets provided large inputs of terrigenous sediments to the slopes, where widespread mass movements prevailed (e.g., Kuhn and Weber, 1993; Pudsey et al., 1988). In the southern Drake Passage-Scotia Sea, higher percentages of terrigenous input and lower percentages of biogenic components characterize depositional environments under extensive se ice and an advanced ice shelf (e.g., Yoon et al., 2007, 2009; Bak et al., 2014; Xiao et al., 2016; Kim et al., 2020) (Fig. 10).

In the study area, several proxies indicate that sedimentological Units IV and III are mainly terrigenous in origin. For example, high elemental counts of Si, K and Al and K/Ti ratios have been related to higher supplies of terrigenous material during glacials (e.g., Rothwell and Croudace, 2015; Bertram et al., 2018). In addition, high K/Ti ratios indicate an increased influx of illite-rich material (e.g., Diekmann et al., 2008) largely supplied by physical weathering (e.g., Diekmann et al., 2000; Marinoni et al., 2008); illite-dominated clay fractions along with higher MS and density values (Figs. 6 and 8B) suggest a close relationship between grain size and physical properties, which also supports a terrigenous depositional regime. Large amounts of fine-grained material likely suggest sediment deposition from the nepheloid layers, where sediments can be supplied by bottom-current erosion, ice rafting and pelagic and/or hemipelagic settling (Stow and Holbrook, 1984; Gonthier et al., 1984; Stow and Faugères, 2008). In contrast, low diatom abundances and Br/Ti ratios attest to limited primary productivity in surface waters (Gersonde et al., 2005; Agnihotri et al., 2008; Bahr et al., 2014). Overall, all these conditions are characteristic of a glacial environment (Vanderaveroet et al., 1999), when high terrigenous influx may have derived from the Antarctic Peninsula's Shelf through ice rafting or from the Weddell Sea via increased input to the benthic nepheloid layer.

Unit IV sediments, moreover, comprise sporadic biogenic (diatom)-rich intervals as well as significant gravity-driven deposits (Fig. 6), including multiple small turbidity events recognized in core TG-03 (e.g., Figs. 7A and 8A). The episodic occurrence of diatom-rich intervals in Unit IV (Fig. 6) indicates mixtures of terrigenous and biogenic-rich components. In the nearby Protector Basin (Fig. 10), comparable diatomaceous mud layers were interpreted as dense turbid bottom current deposits triggered by intensified sea-ice formation in coastal polynyas during the LGM (Yoon et al., 2007). In our study site, a similar interpretation could be invoked, also considering the widespread occurrence of polynyas in the Weddell Sea during the Last Glacial Period (e.g., Smith et al., 2010, and references therein). High-salinity shelf water would form in association with coastal polynyas, while cooling and brine rejection of saline slope waters would trigger downslope flows of dense

waters (i.e., dense shelf-water cascading). The production of downslope flows of dense waters would have reworked sediments previously deposited on the slope, forming turbidity currents. The generation of turbidity currents facilitated by dense shelf water cascading processes has been discussed formerly in the literature (e.g., Huthnance, 1995; Backhaus et al., 1997). The occasional formation of coastal polynyas on the Elephant Island shelf/upper slope by katabatic winds, extended to Ona High (Fig. 11) could have triggered downslope turbidity currents, reworking fine-grained sediment including diatom blooms common to polynyas (Harris, 2000) giving rise to diatom-rich intervals. Dense water cascading on the continental slope north of Elephant Island is also a present-day process, strongly linked with variations in El Niño-Southern Oscillation (ENSO) (Meredith et al., 2003). Furthermore, comparable examples of dense water cascading off the continental shelf have been reported in the western Mediterranean Sea (e.g., Gaudin et al., 2006; Palanques et al., 2006, 2008; Canals et al., 2006, 2009) and the Adriatic Sea (e.g., Bignami et al., 2007; Turchetto et al., 2007; Trincardi et al., 2007a, 2007b; Canals et al., 2009).

During glacial phases, changes in the formation and velocity of Weddell Sea-derived bottom-waters are debated (Lee et al., 2012), as both decreased and increased bottom waters are reported (e.g., Krueger et al., 2012). For example, contourite deposition in the Antarctic Peninsula margin during glacials has been associated with an important southwestward flowing bottom current (e.g., Barker and Camerlenghi, 2002; Lucchi et al., 2002; Lucchi and Rebesco, 2007). Other studies signaled that bottom-current sediment transport/erosion from the Weddell Sea increased during early glacials and were reduced during full glacial conditions (e.g., Krueger et al., 2012). In the Weddell Sea, Weddell Sea-derived bottom-water production likely weakened owing to the isolation of the ice margin from intrusions of warm CDW, which may have resulted in weakly developed-bottom currents along the Weddell Shelf (Pudsey, 1992). In the study area, moderately to well-sorted terrigenous sedimentation therefore might have largely supplied by the westward-flowing WSDW, under a reduced ACC influence related with the northward migration of fronts during the LGM (e.g., Pudsey et al., 1988; Kim et al., 2020), whereas drifting icebergs calved from glaciated fronts contributed large amount of IRDs (Fig. 11).

Biologically, extremely low diatom absolute abundance during the glacial-aged sediments (Fig. 6) is accompanied by increased relative proportion of extinct diatom species (e.g., *Actinocyclus ingens*, *Denticulopsis* sp. and *Rouxia leventerae*), and also increased *Rhizosolenia* spp. (Fig. 9 and Supplementary Tables 1 and 2). This association is similar to that observed in glacial-aged sediments on the Sabrina slope, East Antarctica (Holder et al., 2020). While dominance in sea ice-related diatom species commonly is used as a paleoindicator of sea-ice extent (Gersonde, 1986; Zielinski and Gersonde, 1997) and in the Scotia Sea, has been proven useful to detect sea-ice expansions during glacial periods (e.g., Gersonde et al., 2005; Bak et al., 2014; Collins et al., 2012; Xiao et al., 2016; Kim et al., 2020), this is not observed in the Ona Basin cores. Species commonly associated with sea ice, such as *F. curta,* and *A. actinochilus* (e.g., Armand et al., 2005), are observed during the glacial interval (Fig. 9), but not in proportions greater than those observed in the interglacial interval. This may reflect increased species reworking during the glacial period and preservational differences among species, even within a sea-ice dominated environment. In sum, the abundance and assemblage data suggest extensive sea-ice coverage and limited primary productivity in the southern Ona Basin during the LGM as reported in comparable settings (e.g., Gersonde et al., 2005; Collins et al., 2012; Bak et al., 2014; Xiao et al., 2016; Kim et al., 2020), combined with increased reworking of older sediments (Fig. 11).

5.2.2.2. The deglaciation. As the LGM terminated, the Weddell Sea continental margin deglaciated rapidly and the grounding line retreated

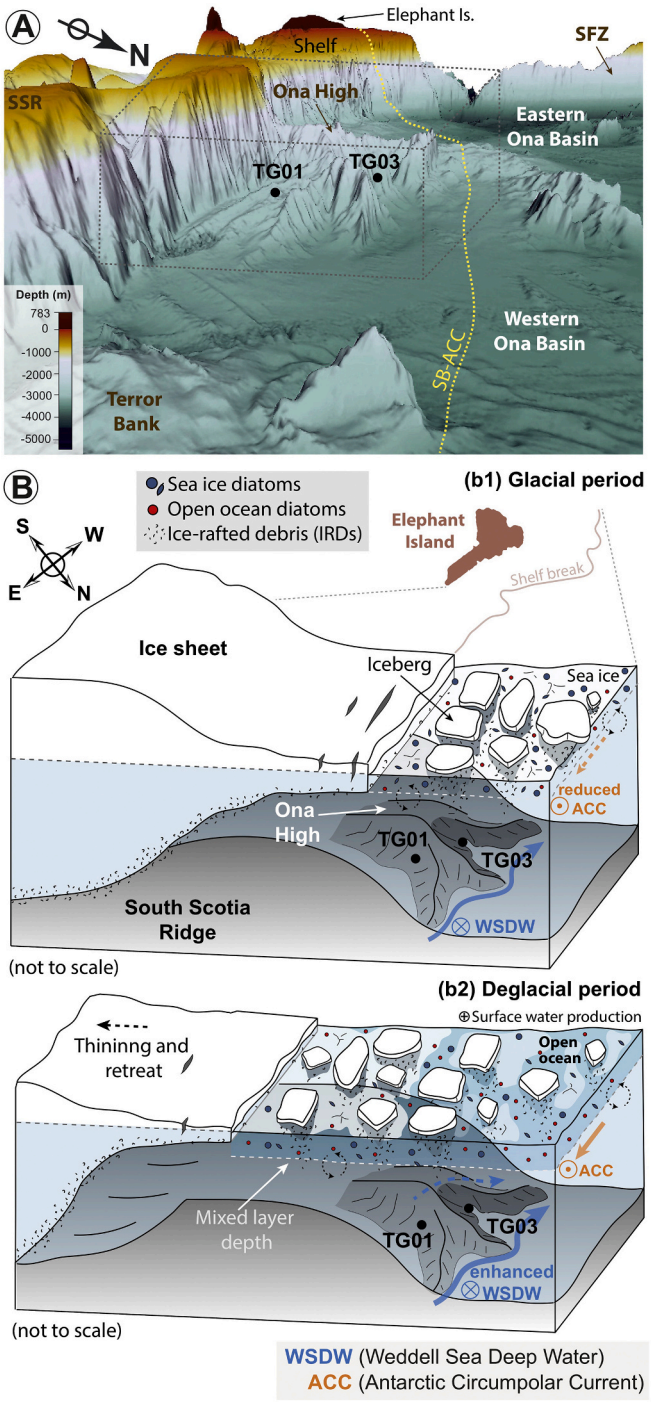

Fig. 11. A) Detailed 3-D bathymetric map of the present-day southern Ona Basin. Bathymetry is extracted from the DBM-BATDRAKE compilation (Bohoyo et al., 2019). Dashed surface area corresponds to the model presented in (B). Location of cores TG-01 and TG-03 and the Southern Boundary of the Antarctic Circumpolar Current (SB-ACC) is shown. SSR: South Scotia Ridge; SFZ: Shackleton Fracture Zone. B) Paleoceanographic model of the southern Ona Basin during the Last Glacial Maximum (LGM) and the subsequent deglaciation. (b1) Glacial period characterized by the progressive ice shelf/sea ice development off the vicinity of Elephant Island. (b2) Deglacial period characterized by sea ice retreat and subsequent increase in open ocean/productivity conditions. The long-term bottom-current strengthening is also shown.

to near its modern position, exposing massive areas of sediment-laden basal ice (see review by Hillenbrand et al., 2014, and references therein). In the southern Scotia Sea, the sea ice retreat favored open ocean conditions, enhancing surface water productivity (Bak et al., 2014; Xiao et al., 2016; Kim et al., 2020). During the deglaciation, all oceanic fronts migrated southward, enhancing plankton photosynthesis and, thus, high levels of nutrients in meltwater-induced, low-salinity subsurface waters (Kim et al., 2020). In the southern Drake Passage-Scotia Sea, lower percentages of terrigenous input and higher percentages of biogenic components characterize depositional environments under open ocean conditions (e.g., Yoon et al., 2007, 2009; Bak et al., 2014; Xiao et al., 2016; Kim et al., 2020) (Fig. 10).

In the study area, several proxies indicate that sedimentological Units II and I were also deposited under enhanced productivity water conditions. Higher diatom abundances and Br/Ti ratios (Fig. 6) indicate that primary productivity was enhanced in surface waters (Gersonde et al., 2005; Agnihotri et al., 2008; Bahr et al., 2014). Abundant euhedral to sub-spherical barite grains observed at the base of the biogenic-rich Unit II (Fig. 8G and H) likely suggest high levels of primary productivity in the meltwater-induced and low-salinity surface layer of the water column, as the occurrence of marine (authigenic) barite in oxic-pelagic sediments has been related to high-bio productivity regions (Dymond et al., 1992; Paytan and Griffith, 2007).

High diatom absolute abundance (Fig. 6) accompanied by an increase in *F. kerguelensis* and *T. lentiginosa*, both regarded as open-ocean species (Crosta et al., 2005) (Fig. 9), support reduced sea-ice cover and increased open-ocean conditions and surface water productivity in the southern Ona Basin. We postulate that major sea-ice retreat may have allowed the southward migration of the SB-ACC front, thus enhancing the influence of the ACC in surface waters of the southern margin of the basin (Fig. 11). Other relatively common species in the deglacial assemblage include *Chaetoceros* subg. *Hyalochaete* and *T. antarctica* T2 (Fig. 9). Both are observed in high abundance in surface sediments on the eastern side of the Antarctic Peninsula (Spaulding et al., 2020), and are especially significant members of the coastal diatom assemblage of the northeastern tip of the Antarctic Peninsula (Kyrmanidou et al., 2018). Phytoplankton studies across the Drake Passage document their occurrence as cold water Antarctic species (Olguín et al., 2006).

In the sedimentary record, bioturbated diatomaceous mud is commonly interpreted as hemipelagic mud or deep-sea contourites (Stanley and Maldonado, 1981; Stow and Piper, 1984; Rebesco et al., 2014; Stow and Smillie, 2020). Firstly, the rate of deposition of hemipelagic sediments is typically low, with bioturbation keeping pace during deposition and destroying much of the primary sedimentary fabric. Secondly, pervasive bioturbation has long been related as one of the diagnostic criteria in deep-sea contourites (e.g., Stow and Lovell, 1979; Chough and Hesse, 1985; Wetzel et al., 2008; Stow et al., 2002; Rodríguez-Tovar and Hernández-Molina, 2018). Thus, bioturbated mud of contour-current origin is hardly distinguished from hemipelagites. The absence of laminae in our study cores (Figs. 6 and 7), together with high diatom abundance and Br/Ti ratios, and authigenic barite (Figs. 6 and 8G-H), and low contents of Si, K and Al and K/Ti ratios leads us to interpret Units II and I as hemipelagic deposits, formed under reduced terrigenous sedimentation (Rothwell and Croudace, 2015; Monien et al., 2012; Bertram et al., 2018), with a weakened input of illite-rich material (Diekmann et al., 2008). Consequently, depositional processes leading to the formation of Units II and I were mostly driven by the pelagic rain from primary productivity in surface waters under seasonal sea ice conditions. The background hemipelagic deposition was episodically interrupted. For example, large inputs of coarse material (Fig. 6B) and extinct diatoms (> 40% reworked species; Fig. 9B) with well-preserved valves (e.g., see *Trinacria* in Fig. 8J), in the upper part of Unit II in core TG-03, are indicative of gravity-flow deposits. This interpretation is consistent with reported slope instability processes leading to extensive high-density mass movements in the Ona High flanks (López-Quirós et al., 2020).

The connection between changes of current intensity during the passage from glacial to interglacial conditions around Antarctica is not well understood. Some studies initially suggested that ACC flows and lateral sediment transport were stronger during glacial conditions (Diekmann et al., 2000; Pudsey and Howe, 2002). However, the majority of more recent studies relate the strengthening of contour current flows either to the onset of deglaciations (Jimenez-Espejo et al., 2020) or to the establishment of pure interglacial conditions (Presti et al., 2011). To add more complexity, in the Drake Passage-Scotia Sea region contrasting interpretations regarding the current flows involved have been proposed, assuming an overall process of current strengthening. An increased influence of deep-water emanating from the Weddell Sea has been reported during interglacials, resulting in long-distance sediment transport patterns (Lee et al., 2012). However, other studies have recently suggested an increased influence of the ACC flows in the southern Ona Basin due to the southward migration of oceanic fronts; as a consequence, ACC has intensified during the Holocene, affecting the entire water column (Kim et al., 2020).

In the study area, several observations support a long-term bottom-current strengthening: (a) change in deposition from poorly sorted bioturbated diatomaceous mud to moderately sorted diatom-rich silty to sandy mud; and (b) identification of a minor internal discontinuity within HR unit U1 (Fig. 4). We relate the bottom-current intensification to the westward-flowing WSDW, in relation to increased Weddell Sea water export (Lee et al., 2012) and to the southward migration of fronts (Kim et al., 2020); while iceberg calving in Ona Basin likely occurred coeval with rapid ice shelf/sheet break during the deglaciation (Fig. 11). The fact that the studied cores are located at water depths shallower than 3000 m southward of the southernmost boundary of the ACC would be in agreement with that interpretation. At increasing water depths (i.e., higher than 3500 m water depths), ACC influence would be felt at the seafloor, as recently proposed in Ona Basin (Kim et al., 2020). Thus, over a relatively short horizontal distance there would be a seaward change, from WSDW to ACC influence, conditioned by the sloping interphases exhibited by these two water masses in Ona Basin (López-Quirós et al., 2020).

6. Conclusions

Paleoceanographic conditions prevailing in the southwestern Scotia Sea were reconstructed at two different time scales, the late Quaternary and the latest Pleistocene. The high-resolution seismic stratigraphy analysis of the southern Ona Basin demonstrates major fluctuations in the regional bottom-current patterns during the late Quaternary glacial-interglacial cycles. A marked increase in seismic amplitude and erosional character of the sedimentary record is related to major intensifications in the westward WSDW flow, probably due to latitudinal displacements of the interphase between the deeper component of the ACC and the WSDW. The interphase displacement enhanced the erosional capacity of the WSDW flow in the southern margin of the Ona Basin, as the flow was constrained. In addition to bottom current strengthening, an intensified interaction between along- and downslope processes was also evidenced.

Sediment cores in the study area provide a link between regional conditions in the southwestern Scotia Sea and the late Pleistocene paleoceanographic history, through the identification of glacially derived and deglacial open-marine depositional patterns. During the LGM, the multi-proxy approach indicates a terrigenous depositional regime largely supplied by the westward-flowing WSDW, under a reduced ACC influence due to the northward migration of fronts. Low diatom absolute abundance and assemblages suggest extensive sea-ice coverage and limited primary productivity in the southern margin of the basin, combined with increased reworking of older sediments. Drifting icebergs calved from glaciated fronts contributed with large amount of IRDs. During the deglaciation, a change in the depositional

style to hemipelagic sedimentation with an abundant biogenic fraction was evidenced. High diatom abundances accompanied by an increase in open-ocean species support the establishment of a reduced sea-ice cover and increased open-ocean conditions and surface water productivity in the southern basin margin; in addition, iceberg calving likely occurred coeval with rapid ice shelf/sheet break. Those processes were accompanied by a long-term intensification of the westward-flowing WSDW during the deglaciation. The bottom-current strengthening is related to increased Weddell Sea water export and the southward migration of fronts due to major sea-ice retreat, enhancing the influence of the ACC in surface waters, and thus, affecting the sloping interphase between the deeper component of the ACC and the WSDW.

Supplementary data to this article can be found online at https://doi.org/10.1016/j.margeo.2021.106565.

Data availability

Complete diatom assemblage information is available in the supplementary data to this article. High-resolution seismic data from the Spanish Antarctic research projects are stored at the CNDP - National Antarctic Data Centre and Polar Archive: http://hielo.igme.es/index.php/es/. Physical properties and XRF scanner data of sediment cores TG-01 and TG-03 are available at PANGAEA (López-Quirós et al., 2021, https://doi.pangaea.de/10.1594/PANGAEA.931838).

Declaration of Competing Interest

The authors declare that they have no known competing financial interests or personal relationships that could have appeared to influence the work reported in this paper.

Acknowledgments

Funding for this research was provided by the Spanish Ministry of Science and Innovation (Grant CTM2017-89711-C2-1/2-P) co-financed by the European Regional Development Fund (FEDER). We thank the Commander, officers, crew, and scientific staff of the BIO HESPERIDES for their support in obtaining the data, sometimes under severe sea conditions. We also acknowledge the help of Dr. Rocío Márquez Crespo (Scientific Instrumentation Center, University of Granada) for her assistance using the FESEM. We would also thank Prof. David M. Harwood (University of Nebraska, USA) for helping with diatom identification, and Dr. Ignacio López-Cilla and Luis Galán (Geological Survey of Spain - IGME, Spain) for the analytical support. Prof. Rubens Figueira and Dr. Paulo Ferreira (Oceanographic Institute, University of São Paulo, Brazil) provided useful remarks for age assignments of sediment cores. Seismic interpretations were made using Kingdom Suite™ software, thanks to the participation of the Instituto Andaluz de Ciencias de la Tierra in the IHS University Grant program. We are grateful to the Editor-in-Chief Michele Rebesco, Guest Editor Uisdean Nicholson and to three anonymous reviewers for their valuable suggestions that greatly improved the manuscript.

References

Agnihotri, R., Altabet, M.A., Herbert, T.D., Tierney, J.E., 2008. Subdecadally resolved paleoceanography of the Peru margin during the last two millennia. Geochem. Geophys. Geosyst. 9, Q05013.

Anderson, J.B., Andrew, J.T., 1999. Radiocarbon constraints on ice sheet advance and retreat in the Weddell Sea, Antarctica. Geology 27, 179–182.

Anderson, J.B., Kennedy, D.S., Smith, M.J., Domack, E.W., 1991. Sedimentary facies associated with Antarctica's floating ice masses. In: Anderson, J.B., Ashley, G.M. (Eds.), Glacial Marine Sedimentation; Paleoclimatic Significance, vol. 261. Geological Society of America Special Papers, pp. 1–25.

Anderson, J.B., Shipp, S.S., Lowe, A.L., Wellner, J.S., Mosola, A.B., 2002. The Antarctic ice sheet during the Last Glacial Maximum and its subsequent retreat history: a review. Quat. Sci. Rev. 21, 49–70.

Anderson, J.B., Warny, S., Askin, R.A., Wellner, J.S., Bohaty, S.M., Kirshner, A.E., Livsey, D.N., Simms, A.R., Smith, T.R., Ehrmann, W., Lawver, L.A., Barbeau, D., Wise, S.W., Kulhenek, D.K., Weaver, F.M., Majewski, W., 2011. Progressive Cenozoic cooling and the demise of Antarctica's last refugium. Proc. Natl. Acad. Sci. U. S. A. 108, 11356–11360.

Andrews, J.T., Domack, E.W., Cunningham, W.L., Leventer, A., Licht, K.J., Jull, A.J.T., DeMaster, D.J., Jennings, A.E., 1999. Problems and possible solutions concerning radiocarbon dating of surface marine sediments, Ross Sea, Antarctica. Quat. Res. 52, 206–216.

Armand, L.K., Crosta, X., Romero, O., Pichon, J.-J., 2005. The biogeography of major diatom taxa in Southern Ocean sediments: 1. Sea ice related species. Palaeogeogr. Palaeoclimatol. Palaeoecol. 223, 93–126.

Backhaus, J., Fohrmann, H., Kämpf, J., Rubino, A., 1997. Formation and export of water masses produced in Arctic shelf polynyas — process studies of oceanic convection. ICES J. Mar. Sci. 54 (3), 366–382.

Bae, S.H., Yoon, H.I., Park, B.-K., Kim, Y., 2003. Late Quaternary stable isotope record and meltwater discharge anomaly events to the south of the Antarctic Polar Front, Drake Passage. Geo-Mar. Lett. 23 (2), 110–116.

Baeten, N.J., Laberg, J.S., Forwick, M., 2016. Submarine mass movements affecting contourites on the continental slope offshore of the Lofoten Islands, North Norway. In: Dowdeswell, J.A., Canals, M., Jakobsson, M., Todd, B.J., Dowdeswell, E.K., Hogan, K.A. (Eds.), Atlas of Submarine Glacial Landforms: Modern, Quaternary and Ancient, pp. 397–398.

Bahr, A., Jiménez-Espejo, F.J., Kolasinac, N., Grunert, P., Hernández-Molina, F.J., Röhl, U., Voelker, A.H.L., Escutia, C., Stow, D.A.V., Hodell, D., Alvarez-Zarikian, C. A., 2014. Deciphering bottom current velocity and paleoclimate signals from contourite deposits in the Gulf of Cádiz during the last 140 kyr: an inorganic geochemical approach. Geochem. Geophys. Geosyst. 15, 3145–3160.

Bak, Y.-S., Yoo, K.-C., Yoon, H.I., Lee, J.-D., Yun, H., 2007. Diatom evidence for Holocene paleoclimatic change in the South Scotia Sea, West Antarctica. Geosci. J. 11, 11–22.

Bak, Y.S., Yoo, K.C., Yoon, H.I., 2014. Late quaternary climate changes around the Elephant Islands, antarctic Peninsula. Geosci. J. 18, 495–501.

Barker, P.F., Camerlenghi, A., 2002. Glacial history of the antarctic Peninsula from Pacific margin sediments. In: Barker, P.F., Camerlenghi, A., Acton, G.D., Ramsay, A. T.S. (Eds.), Proc. ODP, Sci. Results, p. 178.

Barker, P.F., Kennett, J.P., Expedition 113 Scientists, 1988. Proceedings of the Ocean Drilling Program, Scientific Results Leg 113. Ocean Drilling Program, p. 774.

Barker, P.F., Camerlenghi, A., Acton, G.D., Expedition 178 Scientists, 1999. Proceedings of the Ocean Drilling Program, Initial Reports, vol. 178. Ocean Drill. Program, College Station, Tex.

Barré, N., Provost, C., Renault, A., Sennéchael, N., 2011. Fronts, meanders and eddies in Drake Passage during the ANT-XX111/3 cruise in January–February 2006: a satellite perspective. Deep-Sea Res. II 58, 2533–2554.

Bentley, M.J., Hodgson, D.A., Smith, J.A., Ó Cofaigh, C., Domack, E.W., Larter, R.D., Roberts, S.J., Brachfeld, S., Leventer, A., Hjort, C., Hillenbrand, C.-D., Evans, J., 2009. Mechanisms of Holocene palaeoenvironmental change in the Antarctic Peninsula region. The Holocene 19 (1), 51–69.

Bentley, M.J., Ó Cofaigh, C., Anderson, J.B., Conway, H., Davies, B., Graham, A.G.C., Hillenbrand, C.-D., Hodgson, D.A., Jamieson, S.S.R., Larter, R.D., Mackintosh, A., Smith, J.A., Verleyen, E., Ackert, R.P., Bart, P.J., Berg, S., Brunstein, D., Canals, M., Colhoun, E.A., Crosta, X., Dickens, W.A., Domack, E., Dowdeswell, J.A., Dunbar, R., Ehrmann, W., Evans, J., Favier, V., Fink, D., Fogwill, C.J., Glasser, N.F., Gohl, K., Golledge, N.R., Goodwin, I., Gore, D.B., Greenwood, S.L., Hall, B.L., Hall, K., Hedding, D.W., Hein, A.S., Hocking, E.P., Jakobsson, M., Johnson, J.S., Jomelli, V., Jones, R.S., Klages, J.P., Kristoffersen, Y., Kuhn, G., Leventer, A., Licht, K., Lilly, K., Lindow, J., Livingstone, S.J., Masse, G., McGlone, M.S., McKay, R.M., Melles, M., Miura, H., Mulvaney, R., Nel, W., Nitsche, F.O., O'Brien, P.E., Post, A.L., Roberts, S. J., Saunders, K.M., Selkirk, P.M., Simms, A.R., Spiegel, C., Stolldorf, T.D., Sugden, D. E., van der Putten, N., van Ommen, T., Verfaillie, D., Vyverman, W., Wagner, B., White, D.A., Witus, A.E., Zwartz, D., The RAISED Consortium, 2014. A community-based geological reconstruction of Antarctic ice sheet deglaciation since the last glacial maximum. Quat. Sci. Rev. 100, 1–9.

Bertram, R.A., Wilson, D.J., van de Flierdt, T., McKay, R.M., Jimenez-Espejo, F.J., Escutia, C., Duke, G., Taylor-Silva, B., Riesselman, C., 2018. Timescales and event sequences of middle to late Pliocene deglaciations in the Wilkes Subglacial Basin. Earth Planet. Sci. Lett. 494, 109–116.

Bignami, F., Sciarra, R., Carniel, S., Santoleri, R., 2007. Variability of Adriatic Sea coastal turbid waters from SeaWiFS imagery. J. Geophys. Res. 112, C03S10.

Bohoyo, F., Galindo-Zaldívar, J., Jabaloy, A., Maldonado, A., Rodríguez-Fernández, J., Schreider, A., Suriñach, E., 2007. Extensional deformation and development of deep basins associated with the sinistral transcurrent fault zone of the Scotia–Antarctic plate boundary. In: Cunningham, W.D., Mann, P. (Eds.), Tectonics of strike- slip restraining and releasing bends. Geological Society of London, Special Publication, London, pp. 203–217. https://doi.org/10.1144/sp290.6.

Bohoyo, F., Larter, R.D., Galindo-Zaldívar, J., Leat, P.T., Maldonado, A., Tate, A.J., Flexas, M.M., Gowland, E.J.M., Arndt, J.E., Dorschel, B., Kim, Y.D., Hong, J.K., López-Martínez, J., Maestro, A., Bermúdez, O., Nitsche, F.O., Livermore, R.A., Riley, T.R., 2019. Morphological and geological features of Drake Passage, Antarctica, from a new digital bathymetric model. J. Maps 15 (2), 49–59.

Canals, M., Puig, P., Durrieu de Madron, X., Heussner, S., Palanques, A., Fabres, J., 2006. Flushing submarine canyons. Nature 444, 354–357.

Canals, M., Danovaro, R., Heussner, S., Lykousis, V., Puig, P., Trincardi, F., Calafat, A.M., Durrieu de madron, X., Palanques, A., Sánchez-Vidal, A., 2009. Cascades in Mediterranean submarine Grand Canyons. Oceanography 22 (1), 26–43.

Cefarelli, A.O., Ferrario, M.E., Almandoz, G.O., Atencio, A.G., Akselman, R., Vernet, M., 2010. Diversity of the diatom genus Fragilariopsis in the Argentine Sea and Antarctic waters: Morphology, distribution and abundance. Polar Biol. 33 (11), 1463–1484.

Chough, S.K., Hesse, R., 1985. Contourites from Eirik Ridge, south of Greenland. Sediment. Geol. 41, 185–199.
Civile, D., Lodolo, E., Vuan, A., Loreto, M.F., 2012. Tectonics of the Scotia-Antarctica plate boundary constrained from seismic and seismological data. Tectonophysics 550-553, 17–34.
Clark, P.U., Shakun, J.D., Baker, P.A., Bartlein, P.J., Brewer, S., Brook, E., Carlson, A.E., Cheng, H., Kaufman, D.S., Liu, Z., Marchitto, T.M., Mix, A.C., Morrill, C., Otto-Bliesner, B.L., Pahnke, K., Russell, J.M., Whitlock, C., Adkins, J.F., Blois, J.L., Clark, J., Colman, S.M., Curry, W.B., Flower, B.P., He, F., Johnson, T.C., Lynch-Stieglitz, J., Markgraf, V., McManus, J., Mitrovica, J.X., Moreno, P.I., Williams, J.W., 2012. Global climate evolution during the last deglaciation. Proc. Natl. Acad. Sci. 109 (19), E1134–E1142.
Collins, L.G., Pike, J., Allen, C.S., Hodgson, D.A., 2012. High-resolution reconstruction of southwest Atlantic sea-ice and its role in the carbon cycle during marine isotope stages 3 and 2. Paleoceanography 27, PA3217.
Crosta, X., Romero, O., Armand, L.K., Pichon, J.J., 2005. The biogeography of major diatom taxa in Southern Ocean sediments: 2. Open Ocean related species. Palaeogeogr. Palaeoclimatol. Palaeoecol. 223 (1–2), 66–92.
DeConto, R.M., Pollard, D., 2016. Contribution of Antarctica to past and future sea-level rise. Nature 531 (7596), 591–597.
Diekmann, B., Kuhn, G., 1999. Provenance and dispersal of glacial-marine surface sediments in the Weddell Sea and adjoining areas, Antarctica: ice-rafting versus current transport. Mar. Geol. 158 (1), 209–231.
Diekmann, B., Kuhn, G., Rachold, V., Abelmann, A., Brathauer, U., Fütterer, D.K., Gersonde, R., Grobe, H., 2000. Terrigenous sediment supply in the Scotia Sea (Southern Ocean): response to late quaternary ice dynamics in Patagonia and on the Antarctic Peninsula. Palaeogeogr. Palaeoclimatol. Palaeoecol. 162, 357–387.
Diekmann, B., Hofmann, J., Henrich, R., Fütterer, D.K., Röhl, U., Wei, K.-Y., 2008. Detrital sediment supply in the southern Okinawa Trough and its relation to sea level and Kurishio dynamics during the late Quaternary. Mar. Geol. 255, 83–95.
Doherty, J.M., Thibodeau, B., 2018. Cold water in a warm world: investigating the origin of the Nordic Seas' unique surface properties during MIS 11. Front. Mar. Sci. 5.
Domack, E.W., Jull, A.J.T., Anderson, J.B., Linick, T.W., Williams, C.R., 1989. Application of tandem accelerometer mass-spectrometer dating to late Pleistocene-Holocene sediments of the East Antarctic continental shelf. Quat. Res. 31, 277–278.
Domack, E.W., Leventer, A., Dunbar, R., Taylor, F., Brachfeld, S., Sjunneskog, C., ODP Leg 178 Scientific Party, 2001. Chronology of the Palmer deep site, Antarctic Peninsula: a Holocene paleoenvironmental reference for the circum-Antarctic. Holocene 11, 1–9.
Dymond, J., Suess, E., Lyle, M., 1992. Barium in deep-sea sediment: a geochemical proxy for paleoproductivity. Paleoceanography 7, 163–181.
Evangelinos, D., Escutia, C., Etourneau, J., Hoem, F., Bijl, P., Boterblom, W., van de Flierdt, T., Valero, L., Flores, J.-A., Rodriguez-Tovar, F.J., Jimenez-Espejo, F.J., Salabarnada, A., López-Quirós, A., 2020. Late Oligocene- Miocene proto-Antarctic Circumpolar current dynamics off the Wilkes Land margin, East Antarctica. Glob. Planet. Chang. 103221.
Evans, J.A., Pudsey, C.J., Ó Cofaigh, C., Morris, P., Domack, E., 2005. Late Quaternary glacial history, flow dynamics and sedimentation along the eastern margin of the Antarctic Peninsula Ice Sheet. Quat. Sci. Rev. 24, 741–774.
Folk, R.L., 1954. The distinction between grain size and mineral composition in sedimentary-rock nomenclature. J. Geol. 62 (4), 344–359.
Galindo-Zaldivar, J., Jabaloy, A., Maldonado, A., Sanz de Galdeano, C., 1996. Continental fragmentation along the South Scotia Ridge transcurrent plate boundary (NE Antarctic Peninsula). Tectonophysics 258, 275–301.
García, M., Lobo, F.J., Maldonado, A., Hernández-Molina, F.J., Bohoyo, F., Pérez, L.F., 2016. High-resolution seismic stratigraphy and morphology of the Scan Basin contourite fan, southern Scotia Sea, Antarctica. Mar. Geol. 378, 361–373.
Gaudin, M., Berné, S., Jouanneau, J.-M., Palanques, A., Puig, P., Mulder, T., Cirac, P., Rabineau, M., Imbert, P., 2006. Massive sand beds attributed to deposition by dense water cascades in the Bourcart canyon head, Gulf of Lions (northwestern Mediterranean Sea). Mar. Geol. 234, 111–128.
Gersonde, R., 1986. Siliceous microorganisms in sea ice and their record in sediments in the southern Weddell Sea (Antarctica). In: Proceedings of the VIIIth Symposium on Living and Fossil Diatoms, pp. 549–566.
Gersonde, R., Abelmann, A., Brathaeur, U., Becquey, S., Bianchi, C., Cortese, G., Grobe, H., Kuhn, G., Niebler, H.S., Segl, M., Sieger, R., Zielinski, U., Futterer, D.K., 2003. Last glacial sea surface temperatures and sea-ice extent in the Southern Ocean (Atlantic-Indian sector): a multiproxy approach. Paleoceanography 18, 1061. https://doi.org/10.1029/2002PA000809.
Gersonde, R., Crosta, X., Abelmann, A., Armand, L., 2005. Sea-surface temperature and sea ice distribution of the Southern Ocean at the EPILOG last Glacial Maximum circum-Antarctic view based on siliceous microfossil records. Quat. Sci. Rev. 24, 869–896.
Gibson, J.A.E., Trull, T., Nichols, P.D., Summons, R.W., McMinn, A., 1999. Sedimentation of ^{13}C-rich organic matter from Antarctic Sea-ice algae: a potential indicator of past sea ice extent. Geology 27, 331–334.
Golledge, N.R., Menviel, L., Carter, L., Fogwill, C.J., England, M.H., Cortese, G., Levy, R. H., 2014. Antarctic contribution to meltwater pulse 1A from reduced Southern Ocean overturning. Nat. Commun. 5, 5107.
Gonthier, E.G., Faugeres, J.-C., Stow, D.A.V., 1984. Contourite facies of the Faro Drift, Gulf of Cadiz. In: Stow, D.A.V., Piper, D.J.W. (Eds.), Fine-Grained Sediments: Deep-Water Processes and Products, vol. 15. Geological Society of London Special Publication, pp. 275–292.
Gordon, J.E., Harkness, D.D., 1992. Magnitude and geographic variation of the radiocarbon content in Antarctic marine life: implications for reservoir corrections in radiocarbon dating. Quat. Sci. Rev. 11, 697–708.
Gordon, A.L., Huber, B.A., McKee, D., Visbeck, M.H., 2010. A seasonal cycle in the export of bottom water from the Weddell Sea. Nat. Geosci. 3, 551–556.
Goslar, T., Czernik, J., Goslar, E., 2004. Low-energy ^{14}C AMS in Poznan radiocarbon laboratory. Pol. Nucl. Instrum. Meth. B 223-224, 5–11.
Harris, P.T., 2000. Ripple cross-laminated sediments on the East Antarctic Shelf: evidence for episodic bottom water production during the Holocene? Mar. Geol. 170, 317–330.
Heaton, T.J., Koehler, P., Butzin, M., Bard, E., Reimer, R.W., Austin, W.E.N., Ramsey, C. B., Grootes, P.M., Hughen, K.A., Kromer, B., Reimer, P.J., Adkins, J., Burke, A., Cook, M.S., Olsen, J., Skinner, L.C., 2020. Marine20-the marine radiocarbon age calibration curve (0-55,000 cal BP). Radiocarbon 62 (4), 779–820.
Hein, A.S., Hulton, N.R.J., Dunai, T.J., Sugden, D.E., Kaplan, M.R., Xu, S., 2010. The chronology of the Last Glacial Maximum and deglacial events in central argentine Patagonia. Quat. Sci. Rev. 29, 1212–1227.
Heroy, D.C., Anderson, J.B., 2005. Ice-sheet extent of the Antarctic Peninsula region during the Last Glacial Maximum (LGM) – insights from glacial geomorphology. Geol. Soc. Am. Bull. 117, 1497–1512.
Heywood, K.J., Naveira Garabato, A.C., Stevens, D.P., Muench, R.D., 2004. On the fate of the Antarctic Slope Front and the origin of the Weddell Front. J. Geophys. Res. 109, C06021.
Hillenbrand, C.-D., Bentley, M.J., Stolldorf, T.D., Hein, A.S., Kuhn, G., Graham, A.G.C., Fogwill, C.J., Kristoffersen, Y., Smith, J.A., Anderson, J.B., Larter, R.B., Melles, M., Hodgson, D.A., Mulvaney, R., Sugden, D.E., 2014. Reconstruction of changes in the Weddell Sea sector of the Antarctic Ice Sheet since the Last Glacial Maximum. Quat. Sci. Rev. 100, 111–136.
Holder, L., Duffy, M., Opdyke, B., Leventer, A., Post, A., O'Brien, P., Armand, L.K., 2020. Controls since the mid-Pleistocene transition on sedimentation and primary productivity downslope of Totten Glacier, East Antarctica. Paleoceanogr. Paleoclimatol. 35, e2020PA003981.
Huthnance, J.M., 1995. Circulation, exchange and water masses at the ocean margin: the role of physical processes at the shelf edge. Prog. Oceanogr. 35, 353–431.
IPCC, 2019. Special report on the ocean and cryosphere in a changing climate. In: Pörtner, H.O., Roberts, D.C., Masson-Delmotte, V., Zhai, P., Tignor, M., Poloczanska, E., Weyer, N.M. (Eds.), IPCC Intergovernmental Panel on Climate Change: Geneva, Switzerland.
Iriondo, M., 2000. Patagonian dust in Antarctica. Quat. Int. 68, 83–86.
Jimenez-Espejo, F.J., Presti, M., Kuhn, G., Mckay, R., Crosta, X., Escutia, C., Lucchic, R. G., Tolotti, R., Yoshimura, Y., Huertas, M.O., Macrì, P., Caburlotto, A., De Santis, L., 2020. Late Pleistocene oceanographic and depositional variations along the Wilkes Land margin (East Antarctica) reconstructed with geochemical proxies in deep-sea sediments. Glob. Planet. Chang. 184, 103045.
Kim, S., Yoo, K.C., Lee, J.I., Lee, M.K., Kim, K., Yoon, H.I., 2018. Relationship between magnetic susceptibility and sediment grain size since the last glacial period in the Southern Ocean off the northern Antarctic Peninsula - linkages between the cryosphere and atmospheric circulation. Palaeogeogr. Palaeoclimatol. Palaeoecol. 505, 359–370.
Kim, S., Yoo, K.-C., Lee, J.I., Roh, Y.H., Bak, Y.-S., Um, I.-K., Lee, M.K., Yoon, H.I., 2020. Paleoceanographic changes in the Southern Ocean off Elephant Island since the last glacial period: Links between surface water productivity, nutrient utilization, bottom water currents, and ice-rafted debris. Quat. Sci. Rev. 249, 106563.
Kim, S., Polyak, L., Joe, Y.J., Niessen, F., Kim, H.J., Choi, Y., Kang, S.-G., Hong, J.K., Nam, S.-I., Jin, Y.K., 2021. Seismostratigraphic and geomorphic evidence for the glacial history of the Northwestern Chukchi Margin, Arctic Ocean. J. Geophys. Res. Earth Surf. 126, e2020JF006030.
Krueger, S., Leuschner, D.C., Ehrmann, W., Schmiedl, G., Mackensen, A., 2012. North Atlantic Deep Water and Antarctic Bottom Water variability during the last 200ka recorded in an abyssal sediment core off South Africa. Glob. Planet. Chang. 80-81, 180–189.
Kuhn, G., Weber, M.E., 1993. Acoustical characterization of sediments by parasound and 3.5kHz systems: related sedimentary processes on the southeastern Weddell Sea continental slope, Antarctica. Mar. Geol. 113, 201–217.
Kwiek, P.B., Ravelo, A.C., 1999. Pacific Ocean intermediate and deep water circulation during the Pliocene. Palaeogeogr. Palaeoclimatol. Palaeoecol. 154, 191–217.
Kyrmanidou, A., Vadman, K., Ishman, S., Leventer, A., Brachfeld, S., Domack, E., 2018. Late Holocene oceanographic and climatic variability in the Perseverance Drift, northwestern Weddell Sea based on benthic foraminifera and diatoms. Mar. Micropaleontol. 141, 10–22.
Lee, J.I., Bak, Y.S., Yoo, K.C., Lim, H.S., Yoon, H.I., Yoon, S.H., 2010. Climate changes in the South Orkney Plateau during the last 8600 years. Holocene 20 (30), 395–404.
Lee, J.I., Yoon, H.I., Yoo, K.-C., Lim, H.S., Lee, Y.I., Kim, D., Bak, Y.-S., Takuya, I., 2012. Late Quaternary glacial-interglacial variations in sediment supply in the southern Drake Passage. Quat. Res. 78 (1), 119–129.
Legg, S., Briegleb, B., Chang, Y., Chassignet, E.P., Danabasoglu, G., Ezer, T., Gordon, A.L., Griffies, S., Hallberg, R., Jackson, L., Large, W., Ozgokmen, T.M., Peters, H., Price, J., Riemenschneider, U., Wu, W., Xu, X., Yang, J., 2009. Improving oceanic overflow representation in climate models. Bull. Am. Meteorol. Soc. 90.
Leventer, A., Domack, E., Barkoukis, A., McAndrews, B., Murray, J., 2002. Laminations from the Palmer deep: a diatom-based interpretation. Paleoceanography 17, 8002.
López-Quirós, A., Lobo, F.J., Escutia, C., García, M., Hernández-Molina, F.J., Pérez, L.F., Bohoyo, F., Evangelinos, D., Salabarnada, A., Maldonado, A., Naveira Garabato, A. C., 2020. Geomorphology of Ona Basin, southwestern Scotia Sea (Antarctica): Decoding the spatial variability of bottom-current pathways. Mar. Geol. 422, 106113.
López-Quirós, A., Lobo, F.J., Duffy, M., Leventer, A., Evangelinos, D., Escutia, C., Bohoyo, F., 2021. Physical Properties and XRF Scanner Data of Sediment Cores TG-

01 and TG-03, Ona Basin, Southwestern Scotia Sea (Antarctica). PANGAEA. https://doi.pangaea.de/10.1594/PANGAEA.931838.
Lucchi, R.G., Rebesco, M., 2007. Glacial contourites on the Antarctic Peninsula margin: Insight for palaeoenvironmental and palaeoclimatic conditions. In: Viana, A.R., Rebesco, M. (Eds.), Economic and Palaeoceanographic Significance of Contourite Deposits, vol. 276. London, Special Publications, Geological Society, p. 111e127.
Lucchi, R.G., Rebesco, M., Camerlenghi, A., Busetti, M., Tomadin, L., Villa, G., Persico, D., Morigi, C., Bonci, M.C., Giorgetti, G., 2002. Mid-late Pleistocene glacimarine sedimentary processes of a high-latitude, deep-sea sediment drift (Antarctic Peninsula Pacific margin). Mar. Geol. 189, 343–370.
Maldonado, A., Barnolas, A., Bohoyo, F., Galindo-Zaldívar, J., Hernández-Molina, F.J., Lobo, F., Rodríguez-Fernández, J., Somoza, L., Vázquez, J.T., 2003. Contourite deposits in the central Scotia Sea: the importance of the antarctic circumpolar current and the Weddell Gyre flows. Palaeogeogr. Palaeoclimatol. Palaeoecol. 198, 187–221.
Maldonado, A., Bohoyo, F., Galindo-Zaldívar, J., Hernández-Molina, F.J., Jabaloy, A., Lobo, F.J., Rodríguez-Fernández, J., Suriñach, E., Vázquez, J.T., 2006. Ocean basins near the Scotia-Antarctic plate boundary: influence of tectonics and paleoceanography on the Cenozoic deposits. Mar. Geophys. Res. 27, 83–107.
Maldonado, M., Bohoyo, F., Galindo-Zaldívar, J., Hernández-Molina, F.J., Lobo, F.J., Lodolo, E., Martos, Y.M., Pérez, L.F., Schreider, A.A., Somoza, L., 2014. A model of oceanic development by ridge jumping: opening of the Scotia Sea. Glob. Planet. Chang. 123, 152–173.
Marinoni, L., Setti, M., Salvi, C., Lopez-Galindo, A., 2008. Clay minerals in late Quaternary sediments from the south Chilean margin as indicators of provenance and palaeoclimate. Clay Miner. 43 (2), 235–253.
Martos, Y.M., Maldonado, A., Lobo, F.J., Hernández-Molina, F.J., Pérez, L.F., 2013. Tectonics and palaeoceanographic evolution recorded by contourite features in southern Drake Passage (Antarctica). Mar. Geol. 343, 76–91.
Meredith, M.P., Hughes, C.W., Foden, P.R., 2003. Downslope convection north of Elephant Island, Antarctica: Influence on deep waters and dependence on ENSO. Geophys. Res. Lett. 30 (9), 1462.
Monien, D., Kuhn, G., von Eynatten, H., Talarico, F.M., 2012. Geochemical provenance analysis of fine-grained sediment revealing Late Miocene to recent Paleo-Environmental changes in the Western Ross Sea, Antarctica. Glob. Planet. Chang. 96–97, 41–58.
Morozov, E.G., Demidov, A.N., Tarakanov, R.Y., Zenk, W., 2010. Abyssal Channels in the Atlantic Ocean. In: Water Structure and Flows. Springer, 978-90-481-9357-8.
Naveira Garabato, A.C., Heywood, K.J., Stevens, D.P., 2002a. Modification and pathways of Southern Ocean Deep Waters in the Scotia Sea. Deep-Sea Res. I Oceanogr. Res. Pap. 49, 681–705.
Naveira Garabato, A.C., McDonagh, E.L., Stevens, D.P., Heywood, K.J., Sanders, R.J., 2002b. On the export of Antarctic Bottom Water from the Weddell Sea. Deep-Sea Res. II Top. Stud. Oceanogr. 49, 4715–4742.
Ó Cofaigh, C., Dowdeswell, J., Allen, C.S., Hiemstra, J.F., Pudsey, C.J., Evans, J., Evans, D.J.A., 2005. Flow dynamics and till genesis associated with a marine-based Antarctic palaeo-ice stream. Quat. Sci. Rev. 24, 709–740.
Olguín, H.F., Boltovskoy, D., Lange, C.B., Brandini, F., 2006. Distribution of spring phytoplankton (mainly diatoms) in the upper 50 m of the Southwestern Atlantic Ocean (30-61°S). J. Plankton Res. 28 (12), 1107–1128.
Orsi, A.H., Whitworth III, T., Nowlin Jr., W.D., 1995. On the meridional extent and fronts of the Antarctic Circumpolar Current. Deep-Sea Res. I 42, 641–673.
Orsi, A.H., Johnson, G.C., Bullister, J.L., 1999. Circulation, mixing, and production of Antarctic Bottom Water. Prog. Oceanogr. 43, 55–109.
Osti, G., Waghorn, K.A., Waage, M., Plaza-Faverola, A., Ferré, B., 2019. Evolution of contourite drifts in regions of slope failures at eastern Fram Strait. Arktos 5, 105–120.
Owen, M.J., Day, S.J., Leat, P.T., Tate, A.J., Martin, T.J., 2014. Control of sedimentation by active tectonics, glaciations and contourite-depositing currents in Endurance Basin, South Georgia. Glob. Planet. Chang. 123, 323–343.
Palanques, A., Durrieu de Madron, X., Puig, P., Fabrés, J., Guillén, J., Calafat, A., Canals, M., Heussner, S., Bonnin, J., 2006. Suspended sediment fluxes and transport processes in the Gulf of Lions submarine canyons. The role of storms and dense water cascad- ing. Mar. Geol. 234, 43–61.
Palanques, A., Guillén, J., Puig, P., Durrieu de Madron, X., 2008. Storm-driven shelf-to-canyon suspended sediment transport at the southwestern end of the Gulf of Lions. Cont. Shelf Res. 28, 1947–1956.
Palmer, M., Gomis, D., Flexas, M.M., Jorda, G., Jullion, L., Tsubouchi, T.C., Naveira Garabato, A., 2012. Water mass pathways and transports over the South Scotia Ridge west of 50°W. Deep-Sea Res. I 59, 8–24.
Paytan, A., Griffith, E.M., 2007. Marine barite: recorder of variations in ocean export productivity. Deep-Sea Res. II 54, 687–705.
Pelayo, A.M., Wiens, D.A., 1989. Seismotectonics and relative plate motions in the Scotia Sea region. J. Geophys. Res. 94 (B6), 7293–7320.
Pérez, L.F., Maldonado, A., Bohoyo, F., Hernández-Molina, F.J., Vázquez, J.T., Lobo, F.J., Martos, Y.M., 2014. Depositional processes and growth patterns of isolated oceanic basins: the Protector and Pirie basins of the Southern Scotia Sea (Antarctica). Mar. Geol. 357, 163–181.
Pérez, L.F., Maldonado, A., Hernández-Molina, F.J., Lodolo, E., Bohoyo, F., Galindo-Zaldívar, J., 2017. Tectonic and oceanographic control of sedimentary patterns in a small oceanic basin: dove basin (Scotia Sea, Antarctica). Basin Res. 29, 255–276.
Pérez, L.F., Hernández-Molina, F.J., Lodolo, E., Bohoyo, F., Galindo-Zaldívar, J., Maldonado, A., 2019. Oceanographic and climatic consequences of the tectonic evolution of the southern scotia sea basins, Antarctica. Earth-Sci. Rev. 198, 102922.
Pérez, L.F., Jakobsson, M., Funck, T., Andresen, K.J., Nielsen, T., O'Regan, M., Mørk, F., 2020. Late Quaternary sedimentary processes in the Central Arctic Ocean inferred from geophysical mapping. Geomorphology 369, 107309.
Pérez, L.F., Martos, Y.M., García, M., Weber, M.E., Raymo, M.E., Williams, T., Bohoyo, F., Armbrecht, L., Bailey, I., Brachfeld, S., Glüder, A., Guitard, M., Gutjahr, M., Hemming, S., Hernández-Almeida, I., Hoem, F.S., Kato, Y., O'Connell, S., Peck, V.L., Reilly, B., Ronge, T.A., Tauxe, L., Warnock, J., Zheng, X., 2021. Miocene to present oceanographic variability in the Scotia Sea and Antarctic ice sheets dynamics: Insight from revised seismic-stratigraphy following IODP Expedition 382. Earth Planet. Sci. Lett. 553, 116657.
Presti, M., Barbara, L., Denis, D., Schmidt, S., De Santis, L., Crosta, X., 2011. Sediment delivery and depositional patterns off Adélie Land (East Antarctica) in relation to late Quaternary climatic cycles. Mar. Geol. 284, 96–113.
Provost, C., Renault, A., Barré, N., Sennéchael, N., Garçon, V., Sudre, J., Huhn, O., 2011. Two repeat crossings of Drake Passage in austral summer 2006: short-term variations and evidence for considerable ventilation of intermediate and deep waters. Deep-Sea Res. II 58, 2555–2571.
Pudsey, C.J., 1992. Late Quaternary changes in Antarctic Bottom Water velocity inferred from sediment grain size in the northern Weddell Sea. Mar. Geol. 107, 9–33.
Pudsey, C.J., 2000. Sedimentation on the continental rise west of the Antarctic Peninsula over the last three glacial cycles. Mar. Geol. 167, 313–338.
Pudsey, C.J., Evans, J., 2001. First survey of Antarctic sub-ice shelf sediments reveals mid-Holocene ice shelf retreat. Geology 29, 787–790.
Pudsey, C.J., Howe, J.A., 2002. Mixed biosiliceous-terrigenous sedimentation under the Antarctic Circumpolar current, Scotia Sea. Geol. Soc. Lond. Mem. 22 (1), 325–336.
Pudsey, C.J., Barker, P.F., Hamilton, N., 1988. Weddell Sea abyssal sediments: a record of Antarctic bottom water flow. Mar. Geol. 81, 289–314.
Pugh, R.S., McCave, I.N., Hillenbrand, C.-D., Kuhn, G., 2009. Circum-Antarctic age modeling of Quaternary marine cores under the Antarctic Circumpolar Current: ice-core dust-magnetic correlation. Earth Planet. Sci. Lett. 284, 113–123.
Raymo, M.E., Mitrovica, J.X., 2012. Collapse of polar ice sheets during the stage 11 interglacial. Nature 483, 453–456.
Rebesco, M., Hernández-Molina, F.J., Van Rooij, D., Wåhlin, A., 2014. Contourites and associated sediments controlled by deep-water circulation processes: state-of-the-art and future considerations. Mar. Geol. 352, 111–154.
Rodríguez-Tovar, F.J., Hernández-Molina, F.J., 2018. Ichnological analysis of contourites: past, present and future. Earth Sci. Rev. 182, 28–41.
Rothwell, R.G., Croudace, I.W., 2015. Twenty years of XRF core scanning marine sediments: what do geochemical proxies tell us? In: Croudace, I.W., Rothwell, R.G. (Eds.), Micro-XRF Studies of Sediment Cores. Developments in Paleoenvironmental Research. Springer Science + Business Media, Dordrecht, pp. 25–101.
Salabarnada, A., Escutia, C., Röhl, U., Nelson, C.H., McKay, R., Jiménez-Espejo, F.J., Bijl, P.K., Hartman, J.D., Strother, S.L., Salzmann, U., Evangelinos, D., López-Quirós, A., Flores, J.A., Sangiorgi, F., Ikehara, M., Brinkhuis, H., 2018. Paleoceanography and ice sheet variability offshore Wilkes Land, Antarctica – part 1: insights from late Oligocene astronomically paced contourite sedimentation. Clim. Past 14, 991–1014.
Schlesinger, A., Cullen, J., Spence, G., Hyndman, R., Louden, K., Mosher, D., 2012. Seismic velocities on the Nova Scotian margin to estimate gas hydrate and free gas concentrations. Mar. Pet. Geol. 35 (1), 105–115.
Shevenell, A.E., Kennett, J.P., 2002. Antarctic Holocene climate change: a benthic foraminiferal stable isotope record from Palmer Deep. Palaeoceanography 17, 1019.
Shin, J.Y., Kim, S., Zhao, X., Yoo, K.C., Yu, Y., Lee, J.I., Lee, M.K., Yoon, H.I., 2020. Particle-size dependent magnetic properties of Scotia Sea sediments since the last Glacial Maximum: glacial ice-sheet discharge controlling magnetic proxeis. Palaeogeogr. Palaeoclimatol. Palaeoecol. 557, 109906.
Sjunneskog, C., Taylor, F., 2002. Postglacial marine diatom record of the Palmer deep, Antarctic Peninsula (ODP leg 178, site 1098) 1. Total diatom abundance. Paleoceanography 17 (3), 8803.
Smith, J.A., Hillenbrand, C.-D., Pudsey, C.J., Allen, C.S., Graham, A.G.C., 2010. The presence of polynyas in the Weddell Sea during the last Glacial Period with implications for the reconstruction of sea-ice limits and ice sheet history. Earth Planet. Sci. Lett. 296 (3–4), 287–298.
Spaulding, N., Lucas, J., Huber, B.A., Leventer, A., 2020. Ice retreat in the eastern Antarctic Peninsula region: the application of diatoms for understanding climate change. Mar. Micropaleontol. 160, 101896.
Stanley, D.J., Maldonado, A., 1981. Depositional models for fine-grained sediments in the western Hellenic Trench, Eastern Mediterranean. Sedimentology 28, 273–290.
Stow, D.A.V., Faugères, J.-C., 2008. Contourite facies and the facies model. In: Rebesco, M., Camerlenghi, A. (Eds.), Contourites. Elsevier, Amsterdam, pp. 223–256.
Stow, D.A.V., Holbrook, J.A., 1984. North Atlantic contourites: an overview. In: Stow, D. A.V., Piper, D.J.W. (Eds.), Fine-Grained Sediments: Deep-Water Processes and Products, vol. 15. Geological Society of London Special Publication, pp. 245–256.
Stow, D.A.V., Lovell, J.P.B., 1979. Contourites: their recognition in modern and ancient sediments. Earth-Sci. Rev. 14, 251–291.
Stow, D.A.V., Piper, D.J.W., 1984. Deep-water fine-grained sediments: facies models. In: Stow, D.A.V., Piper, D.J.W. (Eds.), Fine-Grained Sediments: Deep-Water Processes and Products, vol. 15. Geological Society of London Special Publication, pp. 611–646.
Stow, D., Smillie, Z., 2020. Distinguishing between Deep-Water Sediment Facies: Turbidites, Contourites and Hemipelagites. Geosciences 10 (2), 68.
Stow, D.A.V., Faugères, J.-C., Howe, J.A., Pudsey, C.J., Viana, A.R., 2002. Bottom currents, contourites and dep-sea sediment drift: current state-of-the-art. In: Stow (Ed.), Deep-Water Contourite Systems: Modern Drifts and Ancient Series, Seismic and Sedimentary Characteristics. Geol. Soc., London, Memoirs, 22, pp. 7–20.

Stow, D.A.V., Hunter, S., Wilkinson, D., Hernández-Molina, F.J., 2008. The nature of contourite deposition. In: Rebesco, M., Camerlenghi, A. (Eds.), Contourites. Elsevier, Amsterdam, pp. 143–156.
Stuart, K.M., Long, D.G., 2011. Tracking large tabular iceberg using the SeaWinds Ku-band microwave scatterometer. Deep-Sea Res. II 58, 1285–1300.
Stuiver, M., Reimer, P.J., Reimer, R.W., 2020. CALIB 8.1.0 [WWW program] at. http://calib.org accessed 2021-01-05.
Sudre, J., Garçon, V., Provost, C., Sennéchael, N., Huhn, O., Lacombe, M., 2011. Short-term variations of deep water masses in Drake Passage revealed by a multiparametric analysis of the ANT-XXIII/3 bottle data. Deep-Sea Res. II 58, 2592–2612.
Tarakanov, R.Y., 2010. Circumpolar bottom water in the Scotia Sea and the Drake Passage. Oceanology 50, 1–17.
Tarakanov, R.Y., 2012. The Scotia Sea and the Drake Passage as an orographic barrier for the Antarctic Circumpolar Current. Oceanology 52, 157–170.
Trincardi, F., Foglini, F., Verdicchio, G., Asioli, A., Correggiari, A., Minisini, S., Piva, A., Remia, A., Ridente, D., Taviani, M., 2007a. The impact of cascading currents on the Bari Canyon System, SW-Adriatic Margin (Central Mediterranean). Mar. Geol. 246, 208–230.
Trincardi, F., Verdicchio, G., Miserocchi, S., 2007b. Sea-floor evidence for the interaction between cascading and along-slope bottom-water masses. J. Geophys. Res. Earth Surf. 112, F03011.
Tucker, M.E., 2001. Sedimentary Petrology: An Introduction to the Origin of Sedimentary Rocks. Blackwell Science Ltd., Oxford, 260 pp.
Turchetto, M., Boldrin, A., Langone, L., Miserocchi, S., Tesi, T., Foglini, F., 2007. Particle transport in the Bari Canyon (southern Adriatic Sea). Mar. Geol. 246, 231–247.
Vanderaveroet, P., Averbuch, O., Deconinck, J.-F., Chamley, H., 1999. A record of glacial/interglacial alternations in Pleistocene sediments off New Jersey expressed by clay mineral, grain-size and magnetic susceptibility data. Mar. Geol. 159, 79–92.
Vaughan, D.G., Marshall, G., Connolley, W.M., Parkinson, C., Mulvaney, R., Hodgson, D. A., King, J.C., Pudsey, C.J., Turner, J., Wolff, E., 2003. Recent rapid regional climate warming on the Antarctic Peninsula. Clim. Chang. 60, 243–274.
Warnock, J.P., Scherer, R.P., 2014. A revised method for determining the absolute abundance of diatoms. J. Paleolimnol. 53 (1), 157–163.
Weber, M.E., Kuhn, G., Sprenk, D., Rolf, C., Ohlwein, C., Ricken, W., 2012. Dust transport from Patagonia to Antarctica – a new stratigraphic approach from the Scotia Sea and its implications for the last glacial cycle. Quat. Sci. Rev. 36, 177–188.
Weber, M., Clark, P., Kuhn, G., et al., 2014. Millennial-scale variability in Antarctic ice-sheet discharge during the last deglaciation. Nature 510, 134–138. https://doi.org/10.1038/nature13397.
Weber, M.E., Raymo, M.E., Peck, V.L., Williams, T., Expedition 382 Scientists, 2019. Expedition 382 Preliminary Report: Iceberg Alley and Subantarctic Ice and Ocean Dynamics. International Ocean Discovery Program.
Weber, M.E., Raymo, M.E., Peck, V.L., Williams, T., IODP Expedition 382 Scientists, 2021. Iceberg Alley and Subantarctic Ice and Ocean Dynamics. Proceedings of the International Ocean Discovery Program, 382: College Station, TX. International Ocean Discovery Program.
Weltje, G.J., Tjallingii, R., 2008. Calibration of XRF core scanners for quantitative geochemical logging of sediment cores: theory and application. Earth Planet. Sci. Lett. 274, 423–438.
Wetzel, A., Werner, F., Stow, D.A.V., 2008. Bioturbation and biogenic sedimentary structures in contourites. In: Rebesco, M., Camerlenghi, A. (Eds.), Contourites. Developments in Sedimentology, vol. 60, pp. 183–202.
Wilson, D.J., Bertram, R.A., Needham, E.F., van de Flierdt, T., Welsh, K.J., McKay, R.M., Mazumder, A., Riesselman, C.R., Jimenez-Espejo, F.J., Escutia, C., 2018. Ice loss from the East Antarctic ice sheet during late Pleistocene interglacials. Nature 561, 383–386.
Wu, S., Kuhn, G., Diekmann, B., Lembke-Jene, L., Tiedemann, R., Zheng, X., Ehrhardt, S., Arz, H.W., Lamy, F., 2019. Surface sediment characteristics related to provenance and ocean circulation in the Drake Passage sector of the Southern Ocean. Deep-Sea Res. I 154, 103135.
Xiao, W., Frederichs, T., Gersonde, R., Kuhn, G., Esper, O., Zhang, X., 2016. Constraining the dating of late quaternary marine sediment records from the Scotia Sea (Southern Ocean). Quat. Geochronol. 31, 97–118.
Yoon, H.I., Park, B.-K., Kim, Y., Kang, C.Y., 2002. Glaciomarine sedimentation and its paleoclimatic implications on the Antarctic Peninsula shelf over the last 15000 years. Palaeogeogr. Palaeoclimatol. Palaeoecol. 185, 235–254.
Yoon, H.I., Khim, B.K., Yoo, K.-C., Bak, Y.S., Lee, J.I., 2007. Late glacial to Holocene climatic and oceanographic record of sediment facies from the South Scotia Sea off the northern Antarctic Peninsula. Deep-Sea Res. II 54, 2367–2387.
Yoon, H.I., Yoo, K.-C., Bak, Y.-S., Lee, Y.I., Lee, J.I., 2009. Core-based reconstruction of paleoenvironmental conditions in the southern Drake Passage (West Antarctica) over the last 150 ka. Geo-Mar. Lett. 29 (5), 309–320.
Zielinski, U., Gersonde, R., 1997. Diatom distribution in Southern Ocean surface sediments (Atlantic sector): implications for paleoenvironmental reconstructions. Palaeogeogr. Palaeoclimatol. Palaeoecol. 129, 213–250.